nanomaterials

MDPI

Article

Simulations of Infrared Reflectivity and Transmission Phonon Spectra for Undoped and Doped GeC/Si (001)

Devki N. Talwar [1,2,*] and Jason T. Haraldsen [1]

[1] Department of Physics, University of North Florida, 1 UNF Drive, Jacksonville, FL 32224-7699, USA; j.t.haraldsen@unf.edu
[2] Department of Physics, Indiana University of Pennsylvania, 975 Oakland Avenue, 56 Weyandt Hall, Indiana, PA 15705-1087, USA
* Correspondence: devki.talwar@unf.edu; Tel.: +1-(724)-762-7719

Abstract: Exploring the phonon characteristics of novel group-IV binary XC (X = Si, Ge, Sn) carbides and their polymorphs has recently gained considerable scientific/technological interest as promising alternatives to Si for high-temperature, high-power, optoelectronic, gas-sensing, and photovoltaic applications. Historically, the effects of phonons on materials were considered to be a hindrance. However, modern research has confirmed that the coupling of phonons in solids initiates excitations, causing several impacts on their thermal, dielectric, and electronic properties. These studies have motivated many scientists to design low-dimensional heterostructures and investigate their lattice dynamical properties. Proper simulation/characterization of phonons in XC materials and ultrathin epilayers has been challenging. Achieving the high crystalline quality of heteroepitaxial multilayer films on different substrates with flat surfaces, intra-wafer, and wafer-to-wafer uniformity is not only inspiring but crucial for their use as functional components to boost the performance of different nano-optoelectronic devices. Despite many efforts in growing strained zinc-blende (zb) GeC/Si (001) epifilms, no IR measurements exist to monitor the effects of surface roughness on spectral interference fringes. Here, we emphasize the importance of infrared reflectivity $R(\omega)$ and transmission $T(\omega)$ spectroscopy at near normal $\theta_i = 0$ and oblique $\theta_i \neq 0$ incidence (Berreman effect) for comprehending the phonon characteristics of both undoped and doped GeC/Si (001) epilayers. Methodical simulations of $R(\omega)$ and $T(\omega)$ revealing atypical fringe contrasts in ultrathin GeC/Si are linked to the conducting transition layer and/or surface roughness. This research provided strong perspectives that the Berreman effect can complement Raman scattering spectroscopy for allowing the identification of longitudinal optical ω_{LO} phonons, transverse optical ω_{TO} phonons, and LO-phonon–plasmon coupled ω^{+}_{LPP} modes, respectively.

Keywords: novel binary carbides; polymorphs; zb GeC/Si (001) epilayers; surface roughness; conducting transition layer; infrared reflectivity/transmission spectroscopy

Citation: Talwar, D.N.; Haraldsen, J.T. Simulations of Infrared Reflectivity and Transmission Phonon Spectra for Undoped and Doped GeC/Si (001). *Nanomaterials* **2024**, *14*, 1439. https://doi.org/10.3390/nano14171439

Academic Editor: Arthur P. Baddorf

Received: 21 August 2024
Revised: 27 August 2024
Accepted: 30 August 2024
Published: 3 September 2024

1. Introduction

Incorporating novel materials and devices into unique electronic architectures has been and still is a strong motivation for achieving the overwhelming advances and innovations in modern society. Within the technology revolution, the search for semiconductors began in the early nineteenth century when two crucial materials, silicon (Si) and germanium (Ge), were discovered [1,2]. Ever since the inception of Ge-based bipolar transistors [3–10] and the subsequent success of Si-built metal-oxide-semiconductor field effect transistors (MOSFETs) [11], many rigorous research efforts have been made to comprehend the essential characteristics of group-IV elemental (C, Si, Ge, and Sn) semiconductors. These endeavors have spearheaded spectacular technological expansion by motivating scientists and engineers to design integrated circuits (ICs), which have led to improvements in the development of complex electronic components on a single chip to create microprocessors.

Currently, more than 95% of electronic devices, all over the world, are either Si-based or prepared on Si wafers. Epitaxial growth of ultrathin films on Si or Si-on-insulator (SOI) has recently offered a natural route of sustained improvement in modern state-of-the-art devices. As technological evolution continues to advance, the performance of very-large-scale integrated (VLSI) circuits and extremely matured knowledge of complementary metal-oxide semiconductors (CMOS) have revolutionized the world of electronics [12–16]. Due to the improved device structures with expanded functionalities and shrinkages in sizes, the need for novel wide-bandgap semiconductor materials has recently [17–22] evolved to create devices for applications in the high-temperature electronics, healthcare, photovoltaic, and automotive industries.

Despite the conceptual constraints of Si to generate light, the Si-centered optical platform has rapidly changed the landscape of photonic integrated circuits (PICs) by offering robust solutions in the areas of telecom, datacom, bio-photonics, and quantum networks [23–46], etc. In the mid-IR range, a wide variety of integrated passive and active photonic devices are instigated due to high refractive-index contrast waveguides on SOI with excellent optical properties of Si. The exploration of novel materials with ultra-low loss and high electro-optic coefficients has also been favorably examined to realize the advanced PICs with monolithically integrated light sources and efficient modulators [23–46]. The concept of achieving direct bandgap group-IV carbides is expected to offer a paradigm shift in Si-photonics concerning the monolithic implementation of light emitters. In this regard, the growth of novel group-IV binary XC (X ≡ Si, Ge, and Sn) materials and their polymorphs [e.g., 3C (cubic or zinc-blende (zb)), 2H, 4H, 6H (hexagonal), 9R, and 15R (rhombohedral) structures] on different substrates has attracted considerable attention by offering entirely new opportunities for bandgap and strain engineering [47–53]. Notable advances have been made in recent years due to the unique and exciting properties of group-IV materials and the broad tunability of their structural and electronic characteristics. The XC materials with high optical quality, different bandgaps E_g, hardness, high stiffness, melting point, and high thermal conductivity [47,48] are considered particularly favorable for different applications in blue/ultraviolet (UV) light-emitting diodes (LEDs), laser diodes (LDs), photodetectors, temperature sensors, wear-resistant protective coatings in IR optics, and solar cells [49–53], etc. Due to significant lattice mismatch and differences in the thermal expansion coefficients between the zb XC epilayers and Si substrate, one might expect the possibility of observing structural and/or intrinsic defects near the interfaces [27–30]. However, an appropriate choice of buffer layer acquiring load through relaxation of mechanical stresses in low dimensional heterostructures (LDHs) could help improve the structural qualities of epitaxially grown multi-quantum wells (MQWs) and superlattices (SLs). There remain a few intrinsic issues that might constrain the design of optoelectronic device structures. Solutions to these problems are not impossible and can be resolved by exploiting suitable experiments, e.g., growth [54–72] characterization [73–79], and evaluating their basic traits by theoretical methods [79–97] using state-of-the-art ab initio methodologies [98–120]. Clearly, these novel materials have several incredible properties that set them apart from other II-VI and III-V compound semiconductors [17–20] and make them particularly relevant for further investigations.

From an experimental standpoint, the pulsed supersonic free jets technique [54–56] was employed earlier for an inverse heteroepitaxial growth of Si on SiC to achieve an excellent quality of multilayer structures. A novel arc plasma C gun source has been incorporated in the molecular beam epitaxy (MBE) to grow ultrathin MQWs and SLs [57–59]. We have achieved a good uniformity of 3C-SiC/Si (001) epifilms using a chemical vapor deposition (CVD) method in a vertical reactor V-CVD configuration by setting different Si/C ratios and growth times from 2 min to 6 h [60]. Ultrahigh UH-CVD, reduced pressure RP-CVD, and metalorganic MO-CVD techniques are also successfully employed for preparing different $Si_{1-x}Ge_xC/Si$, $Ge_{1-x}Sn_xC/Si$, GeC/SiC, and GeC/Si epilayers [61–72]. For commercial applications, the RP-CVD method is preferred over the UH-CVD approach due to the balance between good epitaxial quality and realizing relatively high growth rates [72].

Progress made in the growth of C-based exotic materials has given opportunities to both scientists and engineers to assess valuable information about their essential traits by employing rapid and nondestructive experimental methods. The development of crystalline quality of GeC/Si (001) epifilms is a significant issue for their use in electronic devices. Raman scattering spectroscopy (RSS) and Fourier-transform infrared (FTIR) spectroscopy are widely used to characterize the major SiC (3C, 4H, 6H, 9R, 15R, etc.) polymorphs [73,74]. Between FTIR and RSS, the former technique is considered one of the fastest turnaround methods in the electronic industry for establishing phonons and the structural traits of different polar semiconductor materials (e.g., SiC/Si, GaN/Si, etc.).

In GeC/Si (001) epilayers, due to the considerable (15.5%) difference in the lattice constants between GeC film and Si substrate, one could expect the possibility of crystalline defects. Besides misfit dislocations, stacking faults, twins, and inversion domain boundaries, the most common defects in the vicinity of the GeC/Si interface are voids—also known as pits or cavities. Like SiC, such defects in GeC can be generated by Ge/C diffusion related to Ge-C nucleation. It is, therefore, necessary to find ways to identify such intrinsic impurities which could cause either an interfacial transition layer (TL) and/or surface roughness between the 'air-epifilm' and 'epilyer-substrate'. Earlier, Holm et al. [106] performed IR reflectance measurements on CVD-grown 3C-SiC/Si (001) epilayers with different surface roughnesses. They suggested that rough surfaces are responsible for causing deformation in the reststrahlen band region. Other studies [107–110] also noticed high fringe contrasts below the reststrahlen band and attributed them to the existence of TL. Different theoretical models adopted in the literature [106–110] are inconsistent and need further scrutiny. In this context, it is reasonable to ask whether zb GeC/Si and 3C-SiC/Si (001) epilayers exhibit surface roughness and TL structures linked to native defects.

Earlier, we reported comprehensive measurements of reflectivity/transmission spectra on different V-CVD-grown 3C-SiC/Si (001) samples [60]. A careful analysis was performed exploiting a classical three-phase (air/epifilm/substrate) model by employing an effective medium approximation (EMA) to assess the bonding and structural characteristics. Comparison of the calculated results using a modified model with experimental data has provided an accurate evaluation of the film thickness d, TL d_2, surface roughness δ, δ_2, and electron charge carrier concentration η. In epitaxially grown GeC/Si (001) epilayers, however, no such measurements are available. On the contrary, a few reports exist where the IR absorption and μ-Raman spectroscopy studies are performed on hydrogenated amorphous GeC, *a*-$Ge_{1-x}C_x$:H ultrathin films prepared by radio frequency reactive magnetron sputtering methods [89,90]. Different phonon features associated with Ge-C, Ge-H, Ge-H_2, and Ge-CH_n bonds have been assigned. Considering diamondoids as the building blocks of GeC SLs, both IR and RSS studies are used to investigate the impact of nanocrystal size on GeC phonon traits. In the IR measurements, a stretching Ge-C mode is ascribed to the bands appearing between ~610 cm^{-1} and 630 cm^{-1} [90]; however, for the longitudinal optical (ω_{LO}) mode, a wide range of frequencies (~603 cm^{-1}–812 cm^{-1}) is advised for transitions from the nanostructures (diamondoids) to bulk like GeC [89]. Different theoretical calculations exist [79–99] using state-of-the-art ab initio methodologies [98,99]. First-principles calculation of lattice dynamics for zb GeC [83,84] provided atypical values for the transverse optical (ω_{TO}) and ω_{LO} modes. A recent random structure-sampling technique with a density functional theory (DFT) offered ω_{LO} ~750 cm^{-1} and ω_{TO} ~630 cm^{-1} [81] phonons—consistent with our realistic rigid-ion model (RIM) calculations [118].

This paper aims to report methodical simulations (cf. Section 2) of the reflectivity $R(\omega)$ and transmission $T(\omega)$ spectra for GeC/Si (001) epifilms using a classical three-phase model ('air-film-substrate') in an effective medium approximation framework. In the ideal configuration (cf. Section 2.1.1), one expects the heterogenous structure to be perfectly smooth and optically sharp, having parallel interfaces. Due to a significant lattice mismatch of ~15.5% between GeC film and Si substrate, one expects a high density of defects, pits, and/or voids. In the modified model (cf. Figure 1), we have assumed a thin interfacial TL of thickness d_2 near the GeC/Si (001) interface and meticulously included the roughness δ

at the air–GeC surface and δ_2 at the GeC–TL interface. Following Shokhovets et al. [116], the scattering factors χ and χ_2 of the ripples at the interfaces (cf. Section 2.3.1) are carefully incorporated in the modified model. The predicted theoretical results of reflectivity and transmission spectra for the zb GeC/Si (001) epifilms are reported considering various settings by systematically choosing different film thicknesses d, TL d_2, surface roughness δ and δ_2 (cf. Section 3), and doping levels (i.e., charge carrier concentration η), etc. Earlier, by considering an intuitive physical argument, Berreman [121] has demonstrated that in the IR transmission spectrum of a freestanding thin polar film, a minimum occurs at ω_{TO} frequency at the near-normal incidence ($\theta_i = 0$), while in the oblique incidence ($\theta_i \neq 0$) two minima should appear at the ω_{TO} and ω_{LO} phonon frequencies, respectively. Moreover, the author [121] has also argued that the ω_{TO} mode arises in both the s- and p-polarizations, whereas ω_{LO} appears only in the p-polarization. In Sections 3.1–3.3, we have reported our simulated results of $R(\omega)$ and $T(\omega)$ for undoped and n-doped GeC/Si (001) epifilms at near-normal $\theta_i = 0$ and oblique $\theta_i \neq 0$ incidences. In heavily doped semiconductors, the presence of free charge carriers η induces strong interaction between electrons (or holes) and the optical phonons. Such interactions were studied by Raman scattering in III–V epilayers of thicknesses d > 1 μm and η > 5 E+17 cm^{-3} [73–75,122–125]. Experimental results were generally explained by employing two types of interactions: deformation potential and impurity-induced Fröhlich interaction. Here, we report our calculations of ω_{LO} phonon–plasmon modes near $\vec{q} \rightarrow 0$ in a series of heavily doped n-type GeC/Si epifilms. The results are compared/contrasted with the FTIR spectra of 3C-SiC/Si (001) epilayers. The outcomes of our theoretical descriptions are carefully examined in Section 3, with concluding remarks presented in Section 4. The methodical results of $R(\omega)/T(\omega)$ spectra for GeC/Si (001) epilayers offer opportunities for spectroscopists to conduct similar measurements to check our theoretical conjectures.

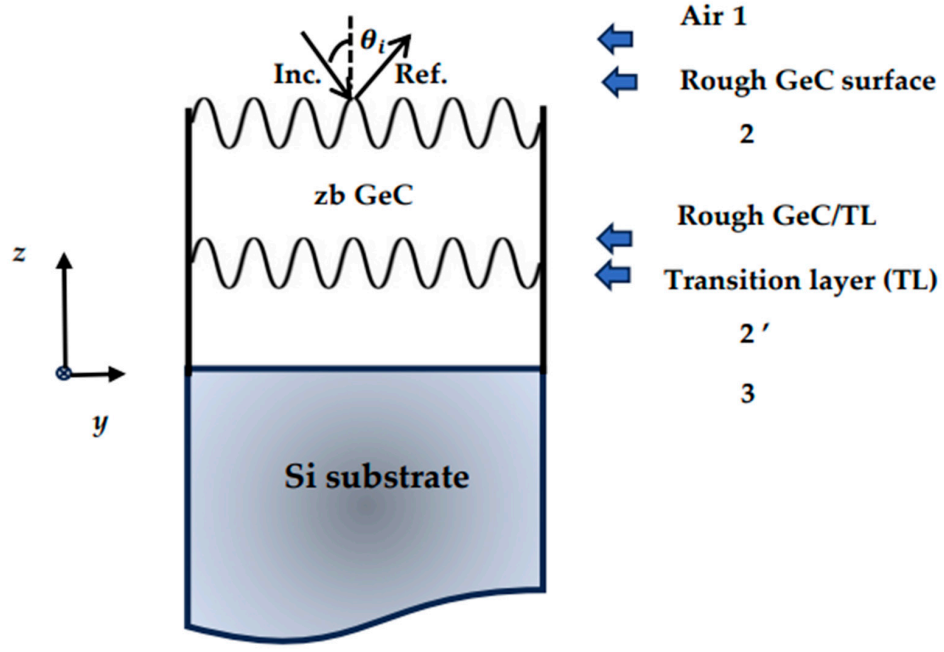

Figure 1. Sketch of a three-phase ideal model ('air/epifilm/substrate') with dielectric functions 1 air $\tilde{\varepsilon}_1 = 1$ (air), 2 $\tilde{\varepsilon}_2 = \tilde{\varepsilon}_{tf}$ (zb GeC thin film), and 3 $\tilde{\varepsilon}_3 = \tilde{\varepsilon}_s$ (Si substrate) for studying the reflectance/transmission spectra of thin zb GeC/Si (001) films grown on a substrate. The modified model with the dielectric functions 1 air $\tilde{\varepsilon}_1 = 1$ (air), $2\tilde{\varepsilon}_2 = \tilde{\varepsilon}_{tf}$ (thin film) transition layer 2′ $\tilde{\varepsilon}' = \tilde{\varepsilon}_{tl}$, and 3 $\tilde{\varepsilon}_3 = \tilde{\varepsilon}_s$ (substrate). Scattering factors χ and χ_2 due to roughness between GeC/air and GeC//TL surface (see Equations (8b,c)) are also included for studying the reflectivity and transmission spectra of thin films grown on a substrate [see text].

2. Theoretical Background

Like 3C-SiC/Si (001), the reflections of IR radiation in GeC/Si (001) epilayers can be described using a complex dielectric function $\tilde{\varepsilon}\left(\vec{q},\ \omega\right)$. In an ideal configuration, one expects the heteroepitaxial structures to be perfectly smooth and optically sharp with parallel interfaces. Thus, our simulation of the infrared reflectivity spectra with interference (cf. Section 2.1) caused by the reflected radiation in GeC/Si (001) epilayers is based on a multi-reflection [96] approach.

2.1. Model for Ideal Structure

Before considering the effects of film thickness d, charge carrier concentration η, phonon/plasmon damping, surface roughness δ, δ_2, interfacial TL d_2, and other factors in the GeC/Si (001) epilayer structures, we start with a conventional EMA methodology by defining the complex dielectric function $\tilde{\varepsilon}\left(\vec{q},\ \omega\right)$ for an ideal bulk material (at $\vec{q} \to 0$) by adopting a 'Drude-Lorentz' model [96]:

$$\tilde{\varepsilon}(\omega) = \varepsilon_\infty\left[1 + \frac{\omega_{LO}^2 - \omega_{TO}^2}{\left(\omega_{TO}^2 - \omega^2 - i\Gamma\omega\right)}\right] - \varepsilon_\infty\left[\frac{\omega_P^2}{\omega(\omega + i\gamma)}\right] = (\varepsilon_1 + i\varepsilon_2) = (n + i\kappa)^2, \quad (1)$$

where ω is the frequency of incident light; ε_∞ is a high-frequency dielectric constant; $\omega_P\left(\equiv\sqrt{\frac{4\pi\eta e^2}{m_e{}^*\varepsilon_\infty}}\right)$ is the characteristic plasma frequency of free conducting electron charge carriers which depends on its concentration η and effective mass $m_e{}^*$; γ (Γ) signifies plasma (phonon) damping coefficient; ω_{TO} (ω_{LO}) symbolizes the TO (LO) phonon frequency near the center of the Brillouin zone (BZ) (i.e., $\vec{q} \to 0$); the mobility μ(η) of free charge carriers is related to $\mu(\eta)(\equiv \frac{e}{m_e{}^*\gamma(\eta)})$.

The dielectric function (cf. Equation (1)) of bulk GeC material can be separated $\tilde{\varepsilon}(\omega)$ $[\equiv \varepsilon_1(\omega) + i\varepsilon_2(\omega)]$ into its real $[\varepsilon_1(\omega)]$ and imaginary $[\varepsilon_2(\omega)]$ parts. The term $\varepsilon_2(\omega)$ represents absorption as a function of ω and affects the reflectivity (transmission) spectrum of the material. Again, $\tilde{\varepsilon}(\omega)$ can be related to real and imaginary parts of the complex refractive index, $\tilde{n}[\equiv n + i\kappa] = \sqrt{\tilde{\varepsilon}}$ [96]:

$$n = \left[\frac{\left({\varepsilon_1}^2 + {\varepsilon_2}^2\right)^{1/2} + \varepsilon_1}{2}\right]^{1/2} \quad (2a)$$

$$\kappa = \left[\frac{\left({\varepsilon_1}^2 + {\varepsilon_2}^2\right)^{1/2} - \varepsilon_1}{2}\right]^{1/2} = \left(\frac{\varepsilon_2}{2n}\right) \quad (2b)$$

where n, κ in Equations (2a) and (2b) are, respectively, the index of refraction and extinction coefficients. The reflectivity R(ω) spectra of bulk zb GeC material can be expressed in terms of their reflectance coefficient $\tilde{r}(\omega)$ [96]:

$$R(\omega) = \left|\tilde{r}(\omega)\right|^2 = \left[\frac{\sqrt{\tilde{\varepsilon}} - 1}{\sqrt{\tilde{\varepsilon}} + 1}\right]^2 = \left[\frac{(n-1)^2 + \kappa^2}{(n+1)^2 + \kappa^2}\right] \quad (3)$$

For simulating R(ω) of GeC/Si (001) epilayers, we have first considered an ideal system (cf. Section 2.2) in the framework of a 'three-phase-model', assuming an ultrathin GeC film deposited on a Si (001) substrate with an abrupt interface. Any interdiffusion that might have occurred during the growth for creating either the TL d_2 and/or surface roughness δ, δ_2, are systematically included in the modified model (cf. Section 2.3). Again, we have expressed here the frequencies of polar modes (ω_{TO}, ω_{LO}) and LO-plasmon coupled phonons in wave number (cm^{-1}). For the GeC epilayer and Si substrate, the values of optical phonons, dielectric constants, phonon damping Γ, and effective electron mass $m_e{}^*$

are taken from the published work (see Table 1) of different research groups [77,78,80,81,86]. As the polar GeC material exhibits distinct ω_{TO}, ω_{LO} modes and can be doped, the two terms on the right-hand side of Equation (1) are significant. On the other hand, as Si substrate is not a polar material (i.e., $\omega_{TO} = \omega_{LO} = 520\ cm^{-1}$ near $\vec{q} \to 0$), only the free charge carriers can interact with IR radiations; hence, the first term in Equation (1) can be neglected.

Table 1. Optical constants of zb GeC and Si materials. The ω_{TO}, ω_{LO} modes and phonon damping Γ are in cm^{-1} for zb GeC and Si. These parameters are used in our calculations of IR reflectivity/transmission of zb GeC/Si (001).

Optical Constants for GeC and Si Material Parameters								
	ε_∞	ω_{TO}	ω_{LO}	Γ	$m_e{}^*$	n_s	n_f	
zb GeC (film)	7.70	626	749	4.5			2.7	Our
	7.29	626	748		0.20 m_e		2.7	Ref. [80]
	7.20	630	755					Ref. [81]
	7.10	682	812					Ref. [86]
Si (substrate)	11.70	520	520			3.42		Refs. [77,78]

2.1.1. Longitudinal-Optical-Phonon–Plasmon Coupling

Raman scattering spectroscopy is commonly used to estimate the charge carrier concentration in doped semiconductors [73–77,122–125]. The RSS in n-doped materials depends on the electron–phonon interaction and is considered an important complement to many other spectroscopic techniques (viz., ellipsometry, luminescence, modulated spectroscopy, photoelectron spectroscopy [73–77,122–125], etc.). One must note that while the phonon describes an elementary excitation of lattice vibration, the plasmon represents the quantization of free electron oscillation. Again, as the lattice vibrations in LDHs are sensitive to local environments, the method can yield information about their microstructural geometry. In RSS, both polarization selection rules and intensity peak positions are sensitive to perturbations, both internal/external, such as strain, electric fields, temperature [73–77,122–125], etc.

In heavily doped semiconductors, including GeC, one can use a simplified approach to determine the carrier concentration η by Raman spectroscopy under non-resonant conditions. As the LO-phonon frequency approaches the plasmon frequency, their interaction instigates the so-called LO phonon–plasmon (LPP) coupled modes, providing two hybrid frequencies: ω^{+}_{LPP} and ω^{-}_{LPP}. The $\omega^{\pm}_{LPP}$ can be obtained from the singularity of the dielectric function (Equation (1), near the center of the BZ (i.e., at $\vec{q} \to 0$) by setting γ and Γ equal to zero [96]:

$$\omega^{\pm}_{LPP} = \left\{ \frac{1}{2} \left[\omega^2_{LO} + \omega^2_P \pm \sqrt{\left(\omega^2_{LO} + \omega^2_P\right)^2 - 4\omega^2_P \omega^2_{TO}} \right] \right\}^{1/2} \quad (4)$$

where $\omega^{+}_{LPP} > \omega_{LO}$ and $\omega^{-}_{LPP} < \omega_{TO}$. From Equation (4), the carrier concentration in doped polar semiconductors can be assessed by investigating the behavior of $\omega^{\pm}_{LPP}$ modes. On the other hand, the simulation of Raman intensity line shapes [125] of the $\omega^{\pm}_{LPP}$ modes are much more complex. Earlier, Kukharskii [126] has theoretically studied the plasmon–phonon coupling in the most conventional GaAs. Experimentally, the observed broadening of the ω_{LO} mode in doped GaAs increases considerably with the increase of η, while the ω_{TO} phonon broadening remains nearly unaffected [125]. In doped semiconductors, the spectral line shapes of LPP modes can be calculated as follows [125]:

$$I_{LPP}\left(\vec{q}, \omega\right) \propto S\left(\vec{q}, \omega\right) \mathrm{Im}\left(-\frac{1}{\tilde{\varepsilon}\left(\vec{q}, \omega\right)} \right) \quad (5)$$

where the response function $S\left(\vec{q}, \omega\right)$ varies between different dominating scattering processes during the Raman studies, including the deformation potential with electro-optic, charge density fluctuation, impurity-induced Fröhlich mechanisms, etc. Detailed expressions involved in $S\left(\vec{q}, \omega\right)$ for various processes can be found in [125]. In the absence of experimental Raman scattering spectroscopy data on the GeC/Si (001), our simulated $R(\omega)$ and $T(\omega)$ in n-doped epilayers of thickness d (μm) revealed distinct minima in the p-polarization (Berreman effect [121]). Given the epilayer thickness, the maxima (minima) are identified as the zone-center ω_{TO} and the high-frequency dip as the ω_{LO} phonon–plasmon coupled mode (cf. Section 3.2.5).

2.2. Ideal Model for GeC/Si (001) Epilayers

In zb GeC, one expects the reststrahlen band (626 cm^{-1}–749 cm^{-1}) of the bulk material to be well separated from the optical phonon frequency (520 cm^{-1}) of the Si substrate. The simulation of IR reflectance (transmission) in the GeC/Si (001) epifilms is one of the bases of multiple reflections in epilayers for causing the interferences between the reflected (transmitted) radiations. Theoretical calculations in a 'three-phase-model' (see Figure 1) can be performed in both the s- and p-polarization using the dielectric functions for the air $\tilde{\varepsilon}_1 = 1$ (air), 2 $\tilde{\varepsilon}_2 = \tilde{\varepsilon}_{tf}$ (zb GeC thin-film), and 3 $\tilde{\varepsilon}_3 = \tilde{\varepsilon}_s$ (Si substrate).

One must note that the s-polarized spectra combine only with the component of the dielectric function parallel to the plane of layers, while the p-polarization spectra couple simultaneously to the components parallel and perpendicular to the plane of layers. The relative contributions of the two (s- and p-) components can be determined (cf. Section 3) from the angle of incidence θ_i. In near-normal conditions ($\theta_i \approx 0$), the total reflectance $R(\omega)$ (transmittance $T(\omega)$) can be expressed as a mean value of the s- and p-polarized reflection (transmission) coefficients [96]:

$$R(\omega) = \frac{\left|\tilde{r}^{2}_{123s} + \tilde{r}^{2}_{123p}\right|}{2} \tag{6a}$$

$$T(\omega) = \frac{\left|\tilde{t}^{2}_{123s} + \tilde{t}^{2}_{123p}\right|}{2} \tag{6b}$$

where $\tilde{r}_{123a}$ ($\tilde{t}_{123a}$) with a (≡s- and p-) are the reflection (transmission) coefficients in the s- and p-polarization, respectively; the numbers 1, 2, and 3 signify the air, film, and substrate in a 'three-phase model' [96]. For an epifilm of thickness d and following Cadman and Sadowski [114], one can evaluate $\tilde{r}_{123a}$ ($\tilde{t}_{123a}$) by using the following:

$$\tilde{r}_{123a} = \frac{\tilde{r}_{12a} + \tilde{r}_{23a}\exp[i2\beta]}{1 + \tilde{r}_{12a}\tilde{r}_{23a}\exp[i2\beta]} \tag{7a}$$

$$\tilde{t}_{123} = \frac{\left(1 + \tilde{r}_{12}\right)\left(1 + \tilde{r}_{23}\right)\exp[i2\beta]}{1 - \tilde{r}_{12}\tilde{r}_{23}\exp[i2\beta]} \tag{7b}$$

in terms of the Fresnel coefficients $\tilde{r}_{ija} = \frac{\tilde{n}_{ia} - \tilde{n}_{ja}}{\tilde{n}_{ia} + \tilde{n}_{ja}}$ and phase multiplier $\beta = 2\pi d\omega\sqrt{\tilde{\varepsilon}_2}$. The above approach to simulate the IR reflectivity (transmission) spectra at near-normal incidence ($\theta_i \approx 0$) in the heteroepitaxial films of thickness d can be extended to oblique incidence ($\theta_i \neq 0$) by using a methodology reported in detail elsewhere [96,112].

2.3. Modified Model for GeC/Si (001) Epilayers

In Equations (6a,b) and (7a,b), we have described a process for simulating the reflectivity (transmission) spectra of an ideal GeC/Si (001) structure where the 'air/epifilm'

surface and 'epifilm/substrate' interface are treated as perfectly smooth and optically sharp. However, the air/epifilm surface and/or interface between film and substrate could be rough, leading to an irregular scattering of the incident radiation [96]. Thus, in a modified model, we need to meticulously include a thin conducting TL of thickness d_2 near the GeC/Si (001) interface and incorporate (cf. Figure 1) the roughness δ near the air–GeC surface and δ_2 between GeC–TL, respectively.

2.3.1. Reflectivity and Transmission

One must note that the perception of surface roughness and 'conducting' TL has been suggested in many surface characterization experiments, e.g., X-ray photoelectron spectroscopy (XPS), inverse photoelectron spectroscopy (IPES), atomic force measurements (AFM), cross-sectional scanning electron microscopy (SEM), and scanning tunneling microscopy (STM) [106,119].

The Rayleigh criterion is commonly used as a test for surface roughness, giving the following critical height (h_c) of surface protuberances [116,117]:

$$h_c = \frac{\lambda}{\cos\theta_i} \tag{8a}$$

where the height (h_c) of a given rough surface is defined as the minimum to maximum surface protuberance. A surface is considered smooth if $h < h_c$ and rough if $h > h_c$. The effects of roughness on IR reflectance can be described by the scattering factors χ and χ_2. From Shokhovets et al. [116] or Landorn et al. [117], the scattering factors of possible ripples at the interfaces (cf. Figure 1) have generally followed the Gaussian distributions:

$$\chi = \exp\left[-8\,(\omega\pi\delta\cos\theta_i)^2\right] \tag{8b}$$

$$\text{and} \quad \chi_2 = \exp\left[-8\,(\omega\pi\delta_2\cos\theta_i)^2\right], \tag{8c}$$

which clearly depend upon the interfacial conditions δ, δ_2 (rms surface roughness in μm) and wavelength λ of the incident photon. At near-normal incidence ($\theta_i \approx 0$), one can calculate the total reflection coefficients $\tilde{r}_{123a}$ and power reflection $R(\omega)\left(\equiv \frac{\left|\tilde{r}^2_{123s}+\tilde{r}^2_{123p}\right|}{2}\right)$ in a modified model using Equations (7a,b) and (8b,c) and following [96]:

$$\tilde{r}_{123a} = \frac{\chi\tilde{r}_{12a} + \chi_2\tilde{r}'_a\exp[i2\beta]}{1+\chi\chi_2\tilde{r}_{12a}\tilde{r}'_a\exp[i2\beta]} \text{ with } \tilde{r}'_a = \frac{\tilde{r}_{22'a} + \tilde{r}_{2'3a}\exp[i2\beta']}{1+\tilde{r}_{22'a}\,\tilde{r}_{2'3a}\exp[i2\beta']} \tag{9}$$

by appropriately including the Fresnel coefficients at the GeC–TL interface along with the phase multiplier β' ($\equiv 2\pi d\omega\sqrt{\tilde{\varepsilon}_{2'}}$). One must note that if the conducting TL layer thickness d_2 and roughness δ, δ_2 approach zero values, the modified model in the EMA transforms into an ideal case. The simulated infrared spectra of GeC/Si (001) epilayers for the ideal and modified structures are compared/contrasted (cf. Section 3) to assess the differences.

3. Numerical Simulations, Results, and Discussion

As stated before, an epifilm prepared on a substrate is comprised of three dielectric constants: air $\varepsilon_{air}(=1)$, thin film $\tilde{\varepsilon}_{tf}(=2)$, and substrate $\tilde{\varepsilon}_s(=3)$ with 'air-film', 'film-substrate', and 'substrate-air' interfaces. To simulate the reflectivity/transmission spectra of V-CVD-grown 3C-SiC/Si (001) samples [60], we considered earlier both the ideal (c.f. Section 2.2) and modified (c.f. Section 2.3) models [96]. The effects of surface roughness and TL played important roles in achieving very good accords with the experimental results. Without such measurements for the GeC/Si (001) epilayers, predictions are made of the

$R(\omega)$ and $T(\omega)$ spectra both at near-normal ($\theta_i = 0$) and oblique incidence ($\theta_i \neq 0$) for undoped and doped films having diverse thicknesses d. In this study, we have confirmed that the Berreman effect [121] in undoped and doped thin films was complementary to Raman scattering spectroscopy for allowing the identifications of ω_{LO}, ω_{TO} phonons as well as LO-plasmon coupled ω^{+}_{LPP} mode, respectively. These results could possibly encourage spectroscopists to examine our theoretical conjectures.

3.1. Reflectivity Spectra of Semi-Infinite zb GeC

Using Equation (3) with appropriate values of phonons and damping parameters (cf. Table 1), we have reported in Figure 2 our simulated reflectivity spectra for undoped and doped semi-infinite GeC. The blue-colored solid line (cf. Figure 2) represents the results of an undoped GeC ($\eta = 0$), and the red-colored solid line indicates the reflectivity spectra of n-type material with the carrier concentration η = 0.5 E+19 cm^{-3}. From the $R(\omega)$ spectra, we have noticed some interesting characteristics: (a) in undoped GeC, the major reststrahlen band (i.e., between ω_{TO} and ω_{LO}) attains a maximum reflectance of ~94% near ω_{TO} 626 cm^{-1}, while a minimum of ~750 cm^{-1} just above ω_{LO} maintains a ~22% value at ω > 1600 cm^{-1}, and (b) for n-type GeC (with η = 0.5 E+19 cm^{-3}) the spectrum indicates two changes from the carrier-free ($\eta = 0$) semi-infinite GeC material: first, the minimum above ω_{LO} (~750 cm^{-1}) is shifted to a higher frequency, and secondly, another minimum appears below ω_{TO}. Obviously, these two features in $R(\omega)$ are linked to the charge carrier concentration and can be exploited to estimate η in doped GeC materials (cf. Section 3.2.2). Again, in the absence of reflectivity studies on bulk GeC, there exist IR absorption and μ-Raman spectroscopy reports on hydrogenated amorphous GeC, *a*-$Ge_{1-x}C_x$:H ultrathin films [89,90]. Using diamondoids as the building blocks of SLs, the ω_{TO} mode ascribed to the vibration of Ge-C appearing between ~610 cm^{-1} and 630 cm^{-1} [90] is in good agreement with our reflectivity calculation.

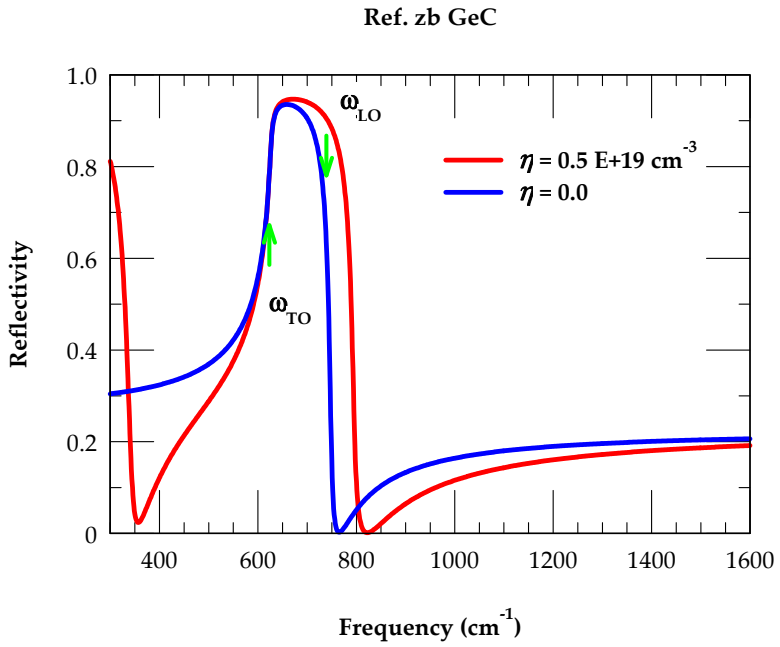

Figure 2. Calculated reflectance spectra at near-normal incidence for semi-infinite n-type zb GeC. The blue and red lines reflect the spectra for undoped $\eta = 0$ and n-doped with η = 0.5 E+19 cm^{-3}, respectively. The positions of ω_{TO} and ω_{LO} modes of zb GeC are also marked (see text).

3.2. Infrared Spectra of GeC/Si (001) Epifilms

In any epifilm/substrate sample, the top and bottom surfaces of the film are expected to reflect light. The total reflected light can depend on two reflections, which add up constructively or destructively depending on their phase relationship. This phenomenon

is related to the wavelike nature of light, with the phase determined by the difference in optical path lengths of the two reflections. Moreover, the resulting interference pattern (fringes) at high frequency can be used to determine film thickness, provided that the refractive index and angle of incidence are known.

3.2.1. Calculated Infrared Reflectance (Transmission) for Ideal GeC/Si (001)

Following the methodology outlined in Section 2.2 with parameter values from Table 1, we have reported our calculated reflectivity and transmission spectra for GeC/Si (001) epilayers. The impact of film thickness, phonon (plasma) damping, and LO phonon–plasmon coupling on the spectral profiles is carefully studied in ideal situations. In appropriate conditions, we have reported/discussed the significance of our simulated spectra of $R(\omega)$ and $T(\omega)$ in Section 3.2.1. (A), (A1) and (B), (B1), respectively.

(A) Reflectance Spectra: Effect of Film Thickness

In Figure 3a, the results of IR reflectance spectra are displayed for GeC/Si (001) epilayers with different film thicknesses, including the bulk zb GeC material. From the simulated $R(\omega)$ spectrum, we have noticed (see Figure 3a) three frequency regions of interest: (i) $\omega < \omega_{TO}$, (ii) between ω_{TO} and ω_{LO} (reststrahlen band), and (iii) $\omega > \omega_{LO}$. The high reflectivity is noticed in the reststrahlen band region of the bulk material, where it reached a maximum ~94% value near $\omega_{TO} \sim 626\ cm^{-1}$, attained its minimum just above ω_{LO} ~750 cm^{-1}, and stayed at a nearly constant ~22% at $\omega > 1600\ cm^{-1}$. In Figure 3a, the simulated $R(\omega)$ results are also displayed for zb GeC/Si (001) epilayers having different thicknesses d between 0.05 μm and 8 μm. Please note that an ultrathin film of thickness d (≡0.05 μm) reveals a sharp and narrow peak near ω_{TO} with no interference fringes, because the optical path difference in the film fails to meet the required interference condition. With increasing the film thickness d between 2 μm and 8 μm, the $R(\omega)$ spectra between the ω_{TO}, ω_{LO} region starts showing well-developed features attaining similarity to bulk-like GeC characteristics along with the interference fringes on both sides of the restsrahlen band.

In a high-frequency region, i.e., $\omega >> \omega_{LO}$, the contrast in the interference fringes [96] varies with the refractive indices of epifilms (n_f) and substrates (n_s), while the film thickness d depends upon the fringe spacing ($\Delta\omega$) and refractive index n_f. In the high-frequency $\omega >> \omega_{LO}$ region, it is possible to approximately calculate the film thickness by using $d \approx (2n_f\Delta\omega)^{-1}$. For a 0.05 μm thick epifilm, our calculated value of $\Delta\omega \approx 37{,}000\ cm^{-1}$ falls well beyond the simulated $R(\omega)$ spectral region with frequency, 400 cm^{-1}–7500 cm^{-1}, which implies that for an ultrathin film, all possible interference extrema are located outside the region of the reflectivity spectrum. As epilayer thickness increases, the corresponding extrema in $R(\omega)$ are seen shifting towards the low-frequency side with the appearance of interference contrasts. For thicker epilayers, it is more appropriate to use a generalized equation $d \approx m/2n_f\Delta\omega$ for obtaining the number of complete cycles m, in the frequency interval $\Delta\omega$. For the GeC/Si (001) epilayers, with $\kappa_f = 0$ and $n_f < n_s$, the values at fringe maxima and minima can be calculated using the following [96,106]:

$$R_{max} = \left[\frac{(n_s - 1)}{(n_s + 1)}\right]^2 \tag{10a}$$

and

$$R_{min} = \left[\frac{(n_s - n_f^2)}{(n_s + n_f^2)}\right]^2 \tag{10b}$$

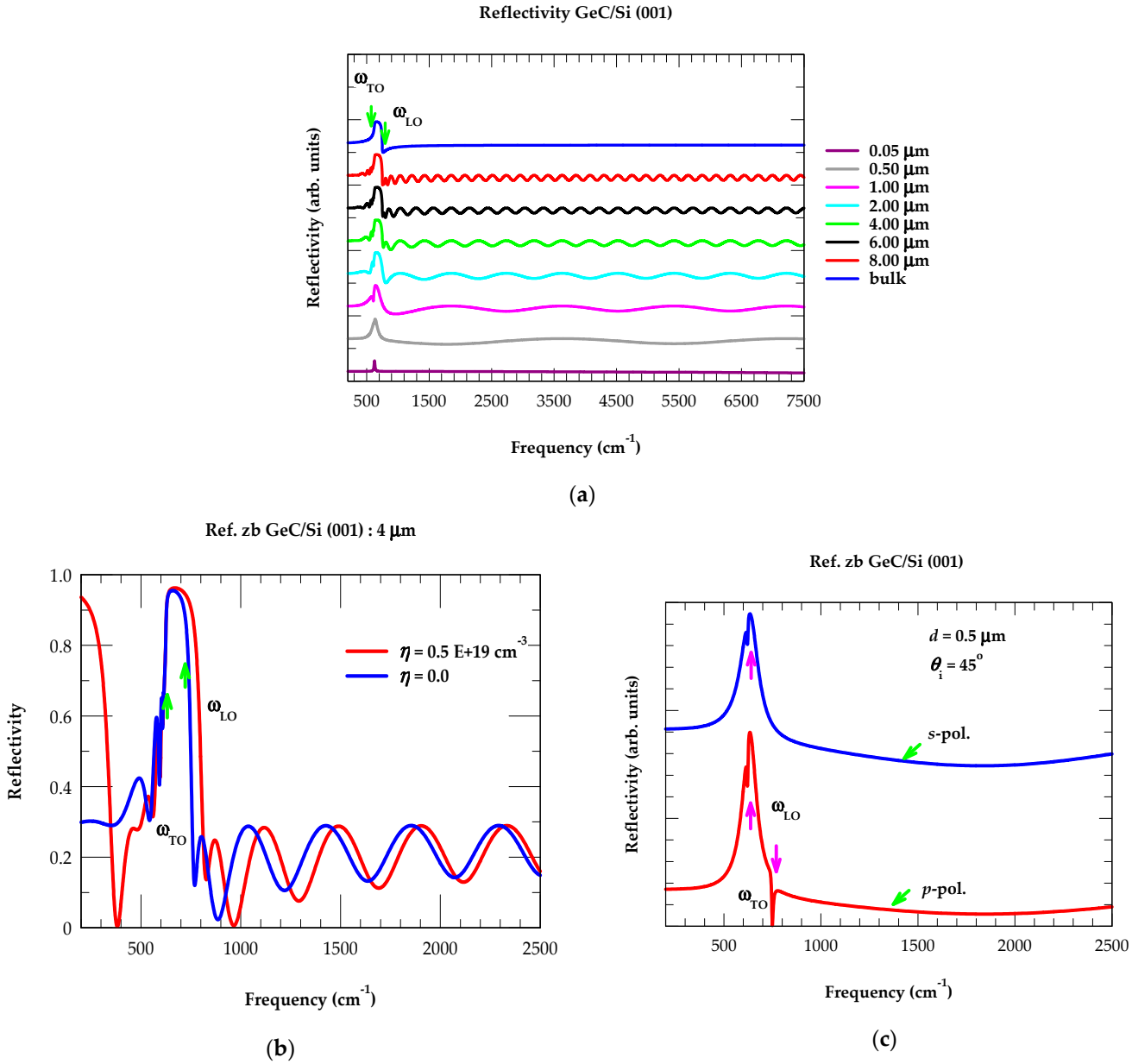

Figure 3. (**a**) Calculated infrared reflectance spectra at near-normal incidence $\theta_i \approx 0$ for the GeC/Si (001) epilayers of different film thicknesses. The results include bulk zb GeC as well as 8 µm, 6 µm, 4 µm, 2 µm, 1 µm, 0.5 µm, and 0.05 µm thick films. (**b**) Reflectivity spectra of 4 µm thick GeC/Si (001) epifilm, with blue- and red-colored lines indicating undoped $\eta = 0$ and n-doped $\eta = 0.5$ E+19 cm^{-3}, respectively. (**c**) Polarization-dependent reflectivity of 0.5 µm thick GeC/Si (001) epifilm at oblique incident angle $\theta_i = 45°$, where blue- and red-colored lines indicate s- and p-polarization spectra. The positions of ω_{TO} and ω_{LO} modes of GeC are also marked (see text).

In a situation with $n_f > n_s$, R_{max} and R_{min} interchange positions. Note that R_{max} in Equation (10a) does not depend on n_f. For $\omega > 1600$ cm^{-1}, the GeC films can be considered lossless with $n_f = 2.7$. For GeC/Si (001) epilayers and ussing the value of n_s from Table 1, one can obtain R_{max}= 30% and R_{min} = 13%, respectively.

(A1) Reflectance Spectra: Effects of Doping

In Figure 3b, we have reported the results of our calculated reflectance spectra at $\theta_i = 0$ for a 4 µm thick GeC/Si (001) epifilm with $\eta = 0$ (blue-colored line: undoped) and $\eta = 0.5$ E+19 cm^{-3} (red-colored line: n-doped). Like $R(\omega)$ of semi-infinite GeC (see

Figure 2), the results of n-doped GeC/Si (001) epifilm revealed two changes from the undoped spectrum (cf. Figure 3b): (a) the minimum above ω_{LO} shifts to a higher frequency, exhibiting a slight separation in the interference fringes initially between 750 and 4000 cm^{-1}, and then starts overlapping at a higher frequency of $\omega > 4000$ cm^{-1}, and (b) a minimum appears with small oscillations below ω_{TO}. We feel that these features can play essential roles in estimating the charge carrier concentration, η in doped epifilms.

In Figure 3c, we have reported our simulated $R(\omega)$ spectra for a 0.5 μm thick GeC/Si (001) epifilm at oblique incidence $\theta_i = 45^\circ$ in the *s*- (blue-colored line) and p-polarization (red-colored line). Comparison with the results at near-normal incidence (i.e., at $\theta_i = 0$, see Figure 3a) spectra has revealed the ω_{TO} frequency in both s- and p-polarization, while ω_{TO} and ω_{LO} modes appear only in the p-polarized spectrum (Berreman effect [121]). We feel that using the reflectivity (cf. Section 3.2.1 (A), (A1)) and/or transmission studies (cf. Section 3.2.1 (B), (B1)) at oblique incidence can allow the direct observation of ω_{LO} mode in undoped epilayers and the LO-plasmon coupled ω^{+}_{LPP} mode in doped samples (c.f. Section 3.2.5).

(B) Transmission Spectra: Effect of Film Thickness

In Figure 4a, we have reported our calculated results of transmission spectra for the GeC/Si (001) epilayers with different thicknesses d (≡0.05 μm–8 μm). For ultrathin film (d ≡ 0.05 μm), the simulated $T(\omega)$ spectra exhibited a sharp dip near ω_{TO} mode frequency with no interference fringes. As the film thickness d steadily increased to 8.0 μm, the calculations revealed deep/flat bands leveling to achieve the GeC bulk-like phonon modes with two extreme edges falling between the reststrahlen band region (i.e., near $\omega_{TO} \sim 626$ cm^{-1} and $\omega_{LO} \sim 750$ cm^{-1}) and interference fringes.

(B1) Transmission Spectra: Effects of Doping

In Figure 4b, the simulated $T(\omega)$ spectra of a 4 μm thick GeC/Si (001) epifilm are displayed at $\theta_i = 0$, for $\eta = 0$ (with blue-colored line indicating undoped) and $\eta = 0.5$ E+19 cm^{-3} (with red-colored line indicating n-doped). Like $R(\omega)$, the transmission spectrum of doped epifilm revealed two modifications from the undoped results (cf. Figure 4b): (a) a minimum above ω_{LO} shifts to a higher frequency with slight separation in interference fringes initially ($\omega <$4000 cm^{-1}), and the fringes start overlapping at $\omega > 4000$ cm^{-1}, and (b) for $\omega < \omega_{TO}$, a minimum appears with small oscillations. In Figure 4c, we have displayed our calculated $T(\omega)$ spectra for a 0.5 μm thick GeC/Si (001) epifilm at $\theta_i = 45^\circ$ in the s- (blue line) and p-polarization (red line). Comparison of the $T(\omega)$ at near-normal incidence (i.e., at $\theta_i = 0$, see Figure 4a) reveals ω_{TO} mode appearing in both s- and p-polarization, while ω_{TO} and ω_{LO} phonons are seen in the p-polarization of the $T(\omega)$ spectrum (Berreman effect [121]). As stated before, the reflectivity and transmission studies (cf. Section 3.2.1 (A), (A1) and (B), (B1)) at oblique incidence allow direct observation of ω_{LO} phonon in undoped epifilms and may permit perceiving the LO-plasmon coupled $\omega^{\pm}_{LPP}$ modes (cf. Section 3.2.5) in doped epilayers.

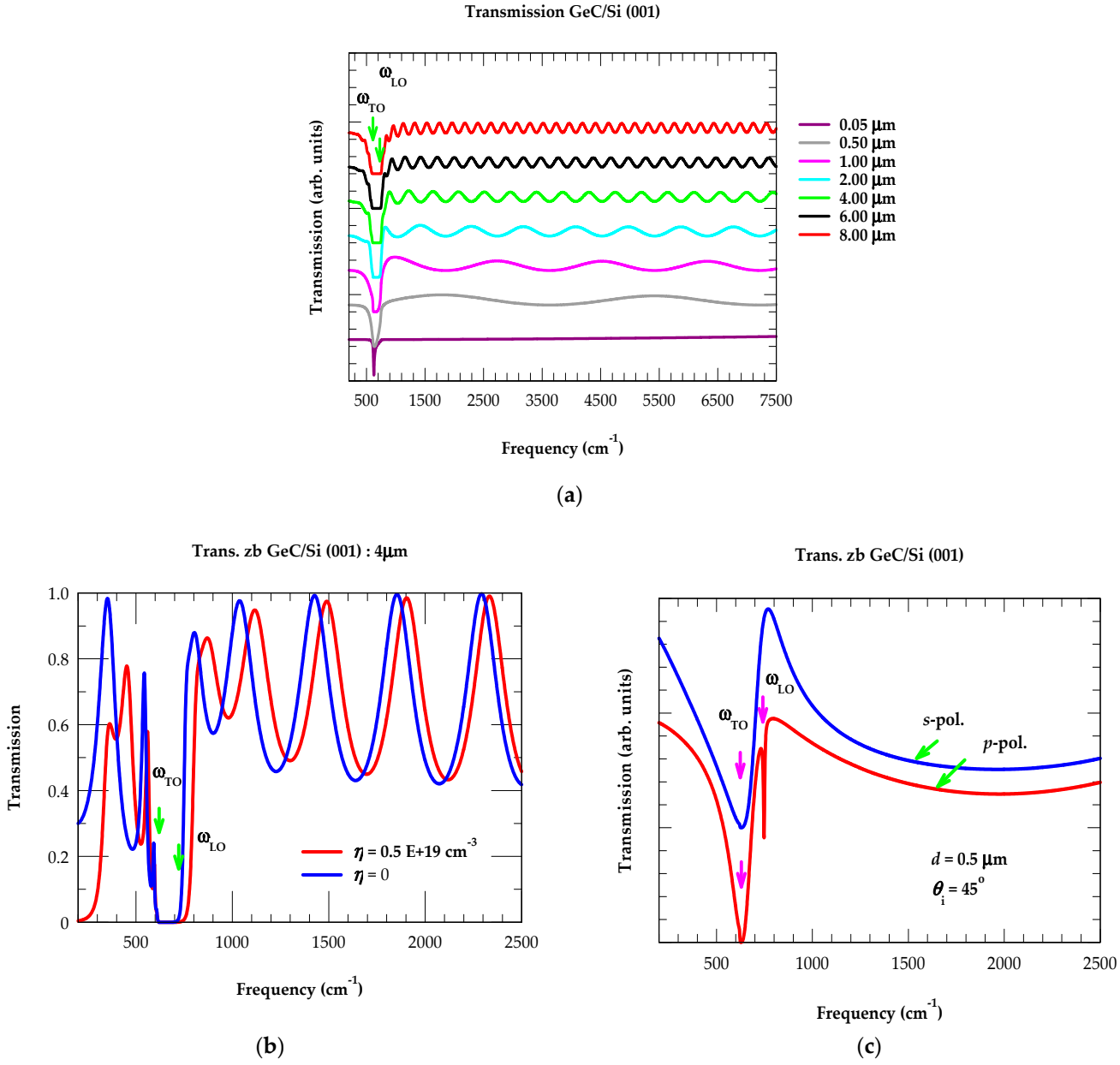

Figure 4. (**a**) Calculated infrared transmission spectra at near-normal incidence $\theta_i \approx 0$ for the GeC/Si (001) epilayers of different film thicknesses. The results include 8 μm, 6 μm, 4 μm, 2 μm, 1 μm, 0.5 μm, and 0.05 μm thick films. (**b**) Transmission spectra of 4 μm thick GeC/Si (001) epifilm, with blue- and red-colored lines indicating undoped $\eta = 0$ and n-doped $\eta = 0.5$ E+19 cm^{-3}, respectively. (**c**) Polarization-dependent transmission spectra of 0.5 μm thick GeC/Si (001) epifilm at oblique incident angle $\theta_i = 45°$, where blue- and red-colored lines indicate s- and p-polarization spectra. The positions of ω_{TO} and ω_{LO} modes of GeC are also marked (see text).

3.2.2. LO-Phonon–Plasma Coupled $\omega^{\pm}_{LPP}$ Modes

For n-type GeC, we have presented in Figure 5 our calculated results of the $\omega^{\pm}_{LPP}$ (green color ω^{+}_{LPP}, magenta color ω^{-}_{LPP}) and ω_P modes (sky blue color) as a function of η. These outcomes are acquired from Equation (1) by setting the real part of the dielectric function, $\widetilde{\varepsilon}(\omega)$, to zero. One must note that for a smaller value of the charge carrier concentration η, the ω^{-}_{LPP} mode near $\vec{q} \to 0$ exhibits a plasmon-like behavior and becomes phonon-like for larger η. On the other hand, the ω^{+}_{LPP} mode with a smaller value of η lies close to ω_{LO} displaying a phonon-like characteristic, which turns into a plasmon-like one

at a higher charge carrier concentration η. In many doped polar semiconductors, extensive Raman scattering and FTIR spectroscopy measurements are reported [73–77,122–125] for identifying LO-plasma coupled phonons.

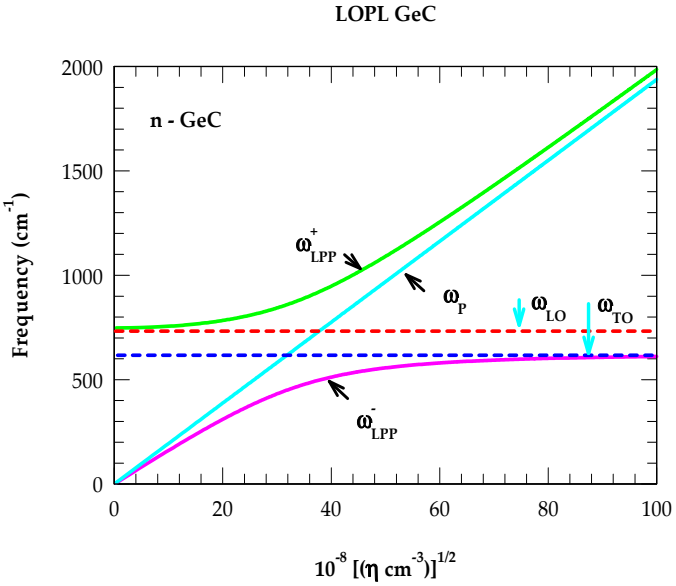

Figure 5. Calculated LO-phonon–plasmon coupled $\omega^{\pm}_{LPP}$ mode frequencies in n-type GeC as a function of free carrier concentration η. The values of ω_{LO}, ω_{TO} modes (dotted lines) of GeC are indicated by sky blue arrows. Variation in ω_P (sky blue line) with η is also displayed (see text).

In Raman scattering spectroscopy, the relative shifts of $\omega^{\pm}_{LPP}$ modes are observed with the broadening of their line widths by increasing η and γ. Thus, only the ω^{-}_{LPP} phonons are detected with a small γ and low η. The ω^{+}_{LPP} mode frequencies are perceived with significantly larger values of γ and η. Moreover, the shifts of ω^{+}_{LPP} phonons to higher energy regions by increasing η cause broader widths with weaker intensities. Obviously, these observations have made the RSS measurements less sensitive [73–77,122–125] for extracting η at higher doping levels. In this context, we strongly feel that the study of p-polarized R(ω) [T(ω)] spectra at oblique incidence (Berreman effect) [121] in doped GeC/Si (001) epifilms (cf. Section 3.2.5) will be valuable for perceiving the modes linked to ω^{+}_{LPP}. In R(ω) [T(ω)], one would also expect the ω^{+}_{LPP} phonons to steadily shift towards higher-frequency regions by increasing η and to help with assessing the accurate values of charge carrier concentration.

3.2.3. Impact of γ, μ, and η on ω_P

In doped polar materials, the plasma damping coefficient $\gamma(\eta)\left(\equiv \frac{e}{m^{*}\mu(\eta)}\right)$ related to the mobility depends upon η via ω_P. In Figure 6a, we have reported the impact of η on ω_P while the dependence of η on μ and γ is displayed in Figure 6b using the empirical relationship of Caughey and Thomas [127]. Consistent with the electrical measurements, our results [see Figure 6b] have revealed a reduction in μ by increasing η. Appropriate parameter values (cf. Table 2) extracted from Figure 6a,b are integrated in Equations (6a,b) and (7a,b) to monitor the effects of η, γ, and ω_P on the R(ω) and T(ω) spectra for the GeC/Si (001) epilayers.

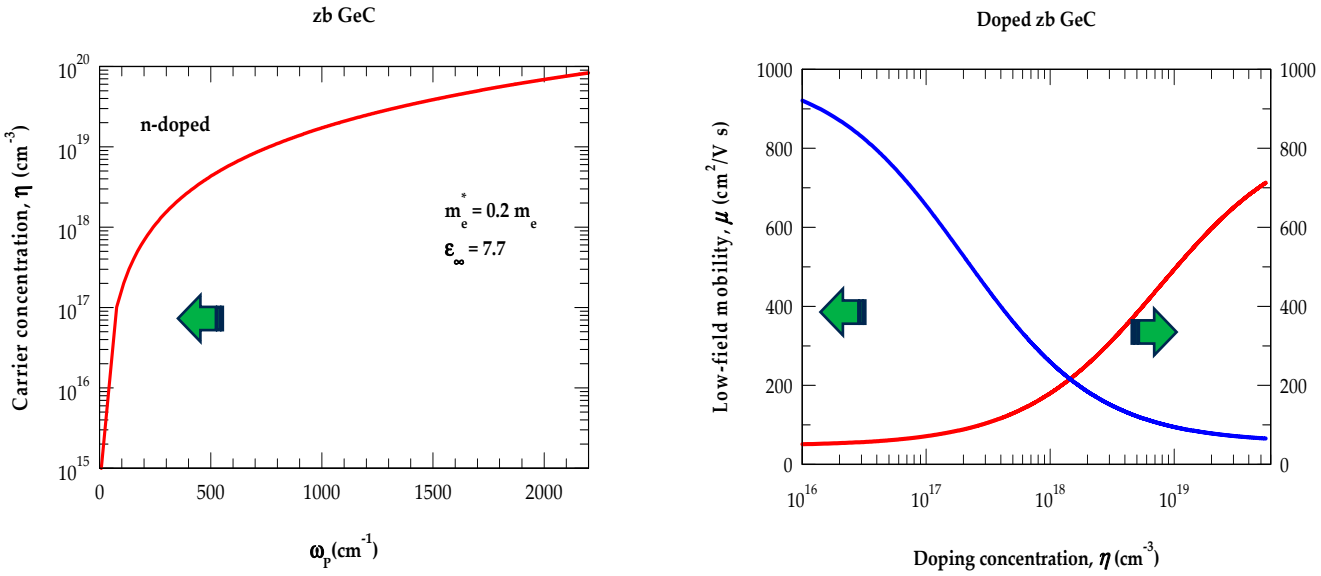

Figure 6. (**a**) Calculated plasma frequency ω_P in cm^{-1} versus charge carrier concentration η (cm^{-3}) in n-type GeC. (**b**) Calculated low field mobility μ in (cm^2/Vs) (left) and plasmon coupling coefficient γ in cm^{-1} versus charge carrier concentration η (cm^{-3}) in n-type GeC (see text).

Table 2. Parameters and their values used for calculating the reflectivity/transmission spectra of n-doped GeC/Si (001) epilayers. The carrier concentration η (E+19 cm^{-3}) dependence on ω_P (cm^{-1}), ω^-_{LPP} (cm^{-1}), and ω^+_{LPP} (cm^{-1}) are estimated from Figures 5 and 6a,b.

Parameters	**GeC**									
η	0.019	0.07	0.16	0.28	0.43	0.62	0.84	1.1	1.7	2.5
ω_P	100	200	300	400	500	600	700	800	1000	1200
ω^-_{LPP}	90	167	241	321	385	442	486	519	561	583
ω^+_{LPP}	750	756	768	787	813	851	901	964	1116	1290

3.2.4. Effects of γ, η, and ω_P on R(ω) and T(ω)

At near-normal incidence (i.e., $\theta_i = 0°$), we have displayed our simulated results (see Figure 7a,b) on a 5 μm thick GeC/Si (001) epifilm, signifying the impacts of γ and ω_P on R(ω) [T(ω)]. The results of reflectance [transmission] spectra in Figure 7a,b are reported by using a constant value of γ = 150 cm^{-1} and varying ω_P from 300 to 1200 cm^{-1}. Three significant changes are revealed (see Figure 7a,b) in the R(ω) [T(ω)] spectra of GeC/Si (001) epifilm: (a) for lightly doped GeC film with ω_P (≡300 cm^{-1}) or η ~1.6 E+18 cm^{-3}, the first minimum [flat] in R(ω) [T(ω)] appears at ~768 cm^{-1} just above ω_{LO}, (b) the reflectance [transmission] becomes much more pronounced [flat] as it shifts toward the higher frequency side with the increase in η or ω_P, and (c) at low-frequency $\omega < \omega_{TO}$ the interference fringes nearly disappear while they have become smaller or even smeared out (1600 cm^{-1} > ω > ω_{LO}) with the increase in ω_P = 1200 cm^{-1} or η ~2.5 E+19 cm^{-3}.

In Figure 7c,d, we have reported the results of R(ω) [T(ω)] by using a constant value of ω_P = 1000 cm^{-1} and varying γ from 100 to 500 cm^{-1}. Clearly, the frequency of ω^+_{LPP} mode near ~1116 cm^{-1} for ω_P = 1000 cm^{-1} (or η ~1.7 E+19 cm^{-3}) remains unaffected while the reflectance [transmission] spectra are changed as we increased the plasma damping constant γ from 100 to 500 cm^{-1}.

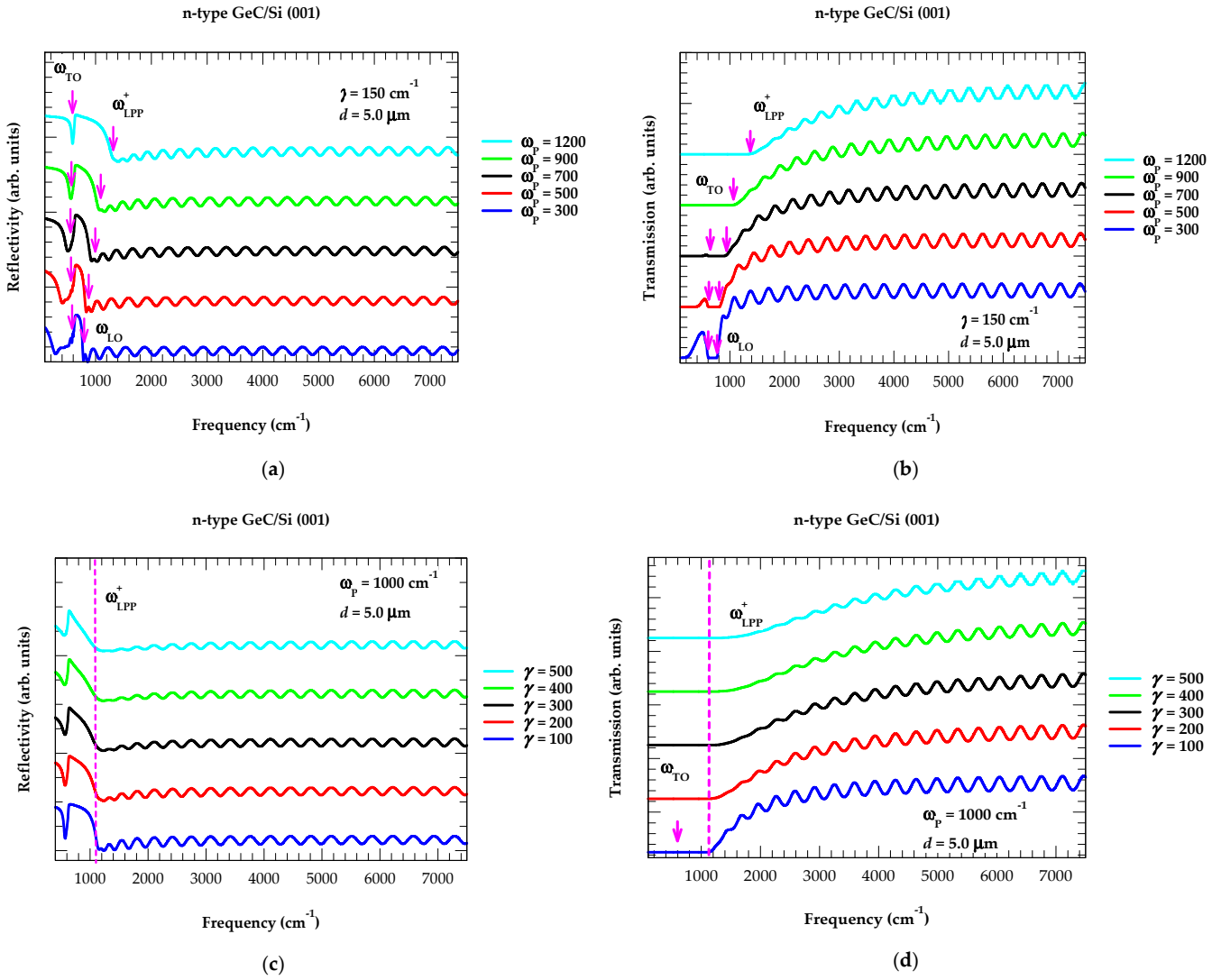

Figure 7. Calculated infrared spectrum of 5.0 μm thick n-type GeC/Si(100) epifilm: (**a**) Reflectivity spectra as a function of frequency (cm^{-1}) for a fixed value of γ = 150 cm^{-1} while changing ω_P from 300, 500, 700, 900, and 1200 cm^{-1}. (**b**) Same key as for (**a**) but for the transmission spectra of 5.0 μm thick n-type GeC/Si(100) epifilm. (**c**) Reflectivity spectra as a function of frequency (cm^{-1}) for a fixed value of ω_P = 1000 cm^{-1} while changing γ from 100, 200, 300, 400, and 500 cm^{-1}. (**d**) Same key as for (**c**) but for the transmission spectra of 5.0 μm thick n-type GeC/Si(100) epifilm (see text).

3.2.5. Berreman's Effect

In Figure 8a,b, we have displayed our calculated results of reflectivity and transmission spectra at oblique incidence (θ_i = 45°) in the s- and p-polarization for a ~1.0 μm thick n-type GeC/Si (001) epifilm having four different charge carrier concentrations η (i.e., 6.2 E+18 cm^{-3}, 1.1 E+19 cm^{-3}, 1.7 E+19 cm^{-3}, and 2.5 E+19 cm^{-3}). The results in p-polarized R(ω) spectra have revealed a maximum at ω_{TO} near ~625 cm^{-1} (see green-colored dotted line) with a dip at the higher frequency (shown by vertical magenta-colored arrows). With the increase in η, this dip clearly shifts from ~851 cm^{-1} → ~964 cm^{-1} → ~1116 cm^{-1} → ~1290 cm^{-1}, respectively. In the s-polarized R(ω) spectra, however, the simulations revealed only a maximum at ω_{TO} near ~625 cm^{-1}, irrespective of the values of η.

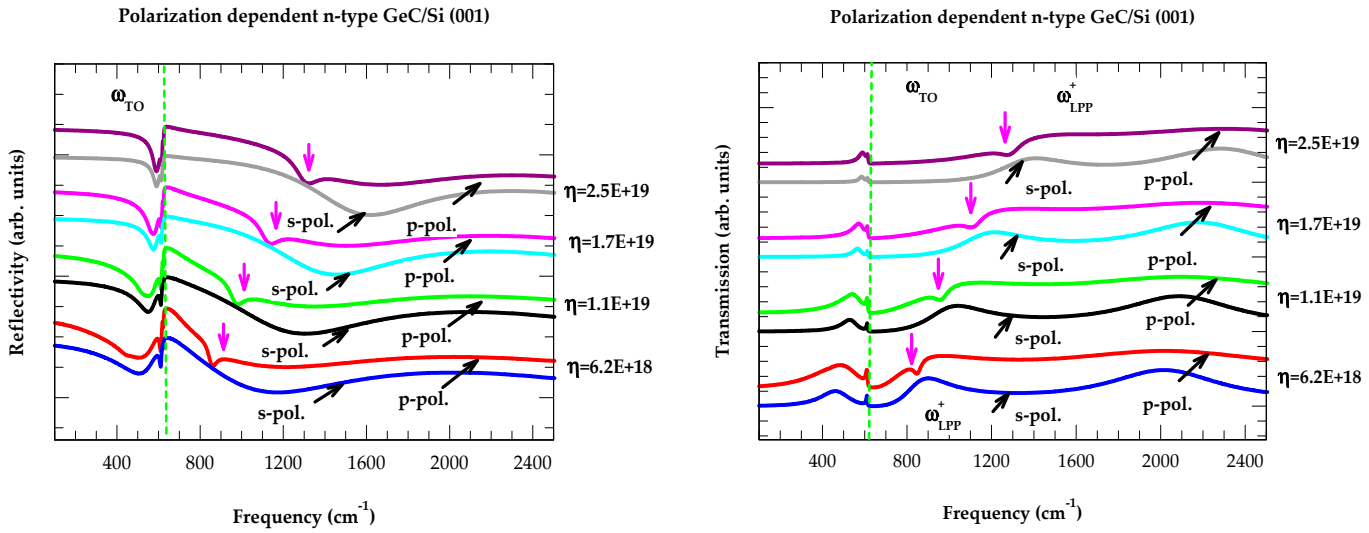

Figure 8. (**a**) Calculated infrared reflectivity spectra at oblique incidence (θ_i = 45°) for n-type GeC/Si (001) 1.0 μm thick film in the s- and p-polarization (different colors). The charge carrier concentration η increased from 6.2 E+18 cm^{-3} → 1.1 E+19 cm^{-3} → 1.7 E+19 cm^{-3} → 2.5 E+19 cm^{-3}, respectively. The calculated shifts of ω^{+}_{LPP} modes in the p-polarization spectra of GeC/Si are shown by the magenta-colored vertical arrows (see text). (**b**) Same key as for (**a**) but for the simulated transmission spectra of 1.0 μm thick epifilm with different charge carrier concentrations η.

By increasing η, our revelation in the p-polarized $T(\omega)$ spectra (see Figure 8b) with a minimum at ω_{TO} ~625 cm^{-1} (green-colored dotted line) and a dip at higher frequency (vertical magenta-colored arrows) have also confirmed its shift from ~851 cm^{-1}→ ~964 cm^{-1} → ~1116 cm^{-1} → ~1290 cm^{-1}, respectively. Like $[R(\omega)]$, the study of $T(\omega)$ has perceived only one [maximum] minimum at ω_{TO} near ~625 cm^{-1} in s-polarization, irrespective of the η values. Therefore, we assigned the high-frequency dips as ω^{+}_{LPP} modes as they shift with the increase of η and emerge only in the p-polarization of the $R(\omega)$ and $T(\omega)$ spectra in oblique geometry (Berreman effect) [121]. These outcomes have indicated that, like RSS, both $R(\omega)$ and/or $T(\omega)$ at oblique incidence can provide alternative means of identifying ω^{+}_{LPP} modes. We strongly feel that these explorations in our findings are valuable for assessing the free charge carrier concentration η in thin n-doped GeC/Si (001) epifilms.

3.3. Modified Model for Infrared Spectra of Epifilms

In GeC/Si (001) epifilms, the assessment of film thickness, free charge carrier concentration, TL, and surface roughness can play critical roles in designing different micro/nanoelectronic device structures. Earlier on, different 3C-SiC/Si (001) epilayers [106–110] and extensive FTIR measurements have helped evaluate valuable information about the roughness at the film–surface and/or film–substrate interface, including the role of conducting TL. However, no such studies are available for the GeC/Si (001) epilayer structures.

Earlier, Pascual et al. [110] have shown that the surface roughness at 3C-SiC film can diminish the average reflectance of interference contrast with the increase in ω. They [110] have also indicated that film–substrate interface roughness may cause a decrease in the relative amplitudes of interference contrasts without affecting the average $\overline{R}(\omega)$ value. In CVD-grown 3C-SiC/Si (001) epilayers, Holm et al. [106] measured $R(\omega)$ spectra with different surface roughnesses, and it was suggested that rough surface can lead to distortion within the reststrahlen band region. By performing AFM measurements on ultrathin 3C-SiC/Si (001) epilayers with film thickness d (≡ 0.82 μm–1.29 μm), Dong et al. [109] have claimed to observe polycrystalline 3C-SiC domains, and within each domain the surface remains nearly flat.

Regarding the impact of film–substate interface roughness, the authors [109] have used cross-sectional SEM and observed a significant number of cavities produced by the interdiffusion of Si and C atoms during carbonization of Si substrate surfaces. While the existence of cavities at the interface can induce light scattering, the authors [109] did not observe their impact on the measured spectral profiles. One may note that the available theoretical analysis considering surface roughness in 3C-SiC/Si epilayers [106–110] is limited to being qualitative.

Our comprehensive measurements of the infrared reflectivity and transmission spectra on V-CVD-grown 3C-SiC/Si (001) samples with film thickness d (≡1.1 μm–20.0 μm) have revealed [60] atypical features exhibiting a decrease in fringe contrasts at higher $\omega > 2000$ cm^{-1}. In most samples, the R(ω) has seen the declining fringe inequalities with a drop in average ($\overline{R}$) value ranging between ~11 and 19%. Obviously, the ideal model (cf. Section 2.1) could not explain the unusual spectral traits. However, we have successfully appraised the observed atypical R(ω)/T(ω) features in 3C-SiC/Si samples using a modified model.

3.3.1. Modified Model for zb GeC/Si (001): Effects of δ and δ_2

For GeC/Si (001) epilayers, we have reported (see Figure 9a,b) our calculated reflectivity results for a 4.0 μm thick film by employing a modified model (cf. Section 2.3). With δ = 0 (cf. Figure 3), the R(ω) spectrum of a 4.0 μm thick GeC epifilm has demonstrated the well-described interference fringe patterns. The effects of increasing δ [δ_2] have revealed, however, high fringe contrasts below the reststrahlen band region (i.e., $\omega < 625$ cm^{-1}) and damping behavior at higher frequency ($\omega > 750$ cm^{-1}). The calculated R(ω) spectra displayed in Figure 9a with blue-, red-, and black-colored lines have considered air–film surface roughness δ ≡ 0.05 μm, 0.10 μm, and 0.15 μm [and in Figure 9b with green-, black-, red, and blue-colored lines of film–substrate interface roughness δ_2 ≡ 0.10 μm, 0.15 μm, 0.20 μm, and 0.25 μm], respectively. Like in the ideal case, we have retained a lower value of η ~1.01 E+17 cm^{-3} in the modified model for simulating the R(ω) spectra with different surface and/or interface roughnesses. With δ = 0 (cf. Figure 3), the R(ω) spectrum of GeC epifilm demonstrated well-described interference fringe patterns. In the modified model, however, the effects of increasing δ have revealed a high fringe contrast below the reststrahlen band and the damping behavior away from the reststrahlen region ($\omega > 1600$ cm^{-1}), exhibiting the increased reduction with downward shifts of the interference fringes. Consistent with our GeC/Si (001) predictions, the observed reflectance R(ω) for the 3C-SiC/Si (001) epilayer with film thickness d (≡1.2 μm) and surface roughness δ (≡0.133 μm: rms value) has revealed [109] comparable trends.

For a 4.0 μm thick GeC/Si (001) epilayer, we have also reported our simulated reflectance R(ω) spectra (see Figure 9b) by carefully including GeC–Si interface roughness δ_2 (≡0.10, 0.15, 0.20, and 0.25 μm). The fringe contrasts at frequencies above the reststrahlen band region in R(ω) are seen steadily decreasing with the increase in δ_2. For δ_2 (≡ 0.25 μm), the values become smaller, even diminishing at $\omega > 7500$ cm^{-1} while retaining reflectance ~22%, as noticed in the semi-infinite GeC at higher ω. For GeC/Si (001) epilayers, our simulated trends in R(ω) agreed reasonably well with the experimental spectra of 3C-SiC/Si (001) epilayers [60,109]. In the epitaxially grown samples, we strongly feel this behavior is caused by optically rough (film–substrate) interfaces where the light scatters diffusely rather than reflecting perfectly.

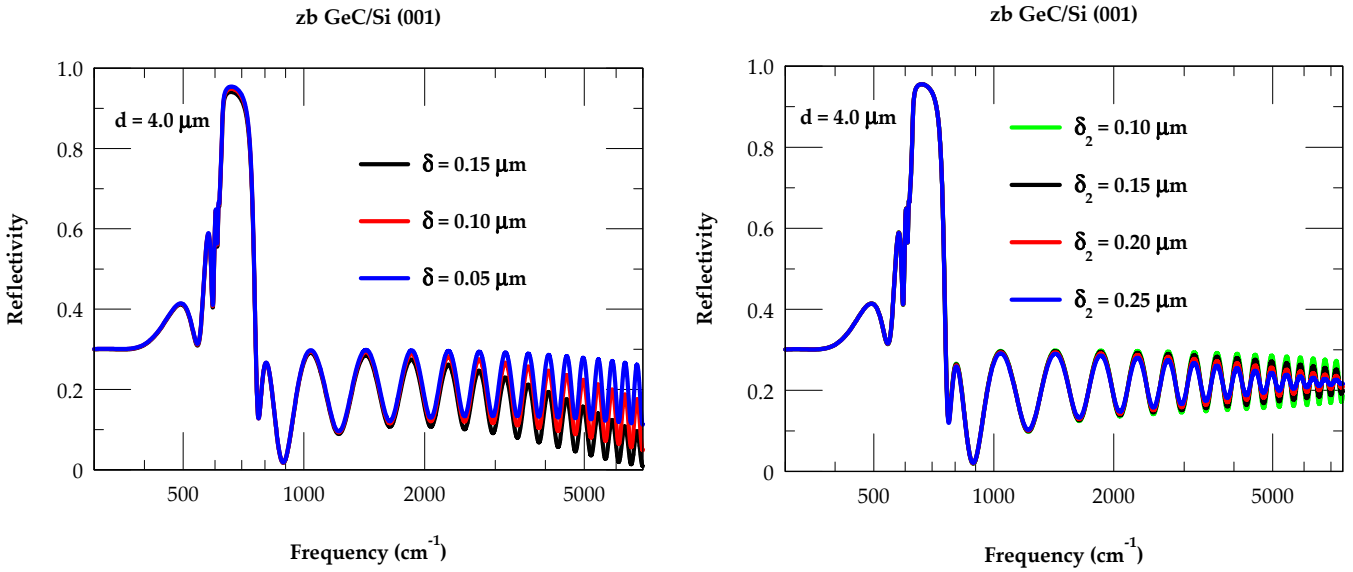

Figure 9. (**a**) Calculated reflectance at near-normal incidence for a 4 μm thick GeC/Si (100) epifilm (η~1.01 E+17 cm^{-3}) with different air/film surface roughnesses δ (≡0.05 μm, 0.10 μm, and 0.15 μm). (**b**) Same key as for (**a**) but for different film/substrate interface roughnesses δ_2 (≡0.10 μm, 0.15 μm, 0.20 μm, and 0.25 μm) (see text).

3.3.2. Modified Model for GeC/Si (001): Effects of δ, δ_2, and TL Thickness

In strained epilayers (e.g., 3C-SiC/Si, GaN/sapphire, InN/Sapphire, etc.), many R(ω) and T(ω) measurements displayed damping behavior in the interference fringe contrast at higher photon energies. These damping traits are either associated with the formation of surface, interfacial roughness, and/or conducting 'graphite-like' TL between the film and substrate. There is a common belief that the relaxation of strain in these epilayer structures accompanies the formation of a high density of intrinsic defects, especially the dislocations. Again, in 3C-SiC/Si (001) epilayers, many TEM and AFM studies have confirmed the presence of a high density of defects near the interface as well as between the film and substrate [60,109]. As the observed damping behavior in interference fringes cannot be explained by exploiting an ideal model, attributing such damping to the formation of interfacial surface roughness δ_2 and/or δ_2+ d_2 (TL) between film–substrate regions supports our assumptions made in the modified model.

By assuming the coexistence of TL d_2(≡ 0.05 μm) and surface [interface] roughness δ [δ_2](≡ 0.10 μm, 0.15 μm, 0.20 μm, and 0.25 μm) in a modified model, we have simulated the reflectivity R(ω) spectra of a 4.0 μm thick film of zb GeC/Si (001) epilayer. While the reflectivity results displayed in Figure 10a,b using green-, black-, red-, and blue-colored lines have exhibited behavior like those of Figure 9a,b, there are a few subtle differences. In agreement with the experimental observations in 3C-SiC/Si epilayers, the effects of (TL+δ) thickness on the R(ω) spectra for zb GeC/Si have exhibited (see Figure 10a) relatively sharp downward shifts (compared to Figure 9a in the interference fringes). The effects of fixed TL d_2 and changing thickness of surface [interface] roughness δ [δ_2] have exhibited a downward shift [reduction in interference fringe contrasts from 12% to 4% near ω ~5100 cm^{-1}] in the reflectivity spectra.

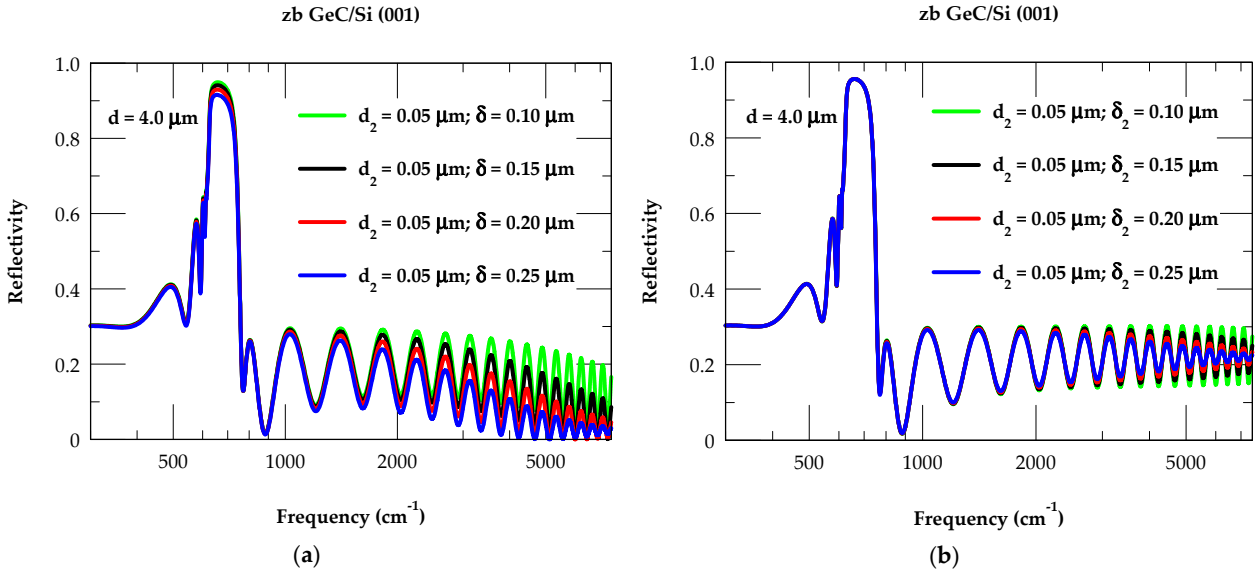

Figure 10. (**a**) Calculated reflectance spectra at near normal incidence ($\theta_i \approx 0$) for a 4 μm thick GeC/Si (100) epifilm (η~1.01 E+17 cm^{-3}) for a fixed value of transition layer thickness $d_2 (\equiv 0.05$ μm) and varying air/film surface roughness δ (≡ 0.10 μm, 0.15 μm, 0.20 μm, and 0.25 μm). (**b**) Same key as for (**a**) with a fixed value of transition layer thickness $d_2 (\equiv 0.05$ μm) and varying film/substrate interface roughness δ_2 (≡ 0.10 μm, 0.15 μm, 0.20 μm, and 0.25 μm) (see text).

4. Concluding Remarks

For novel GeC/Si (001) epilayers, we have reported the results of our comprehensive model-based simulations for IR reflectivity $R(\omega)$ and transmission $T(\omega)$ spectral profiles, at near-normal ($\theta_i \approx 0$) and oblique ($\theta_i \neq 0$) incidence. Different experimental [128] and theoretical methods (viz., Kirchhoff approach, finite element simulation, scalar diffraction, and Rayleigh–Rice theories) exist in the literature to study surface roughness in various materials [129,130]. While scanning probe microscopy and near-field optical microscopy are being used to obtain high-resolution optical images to study surface roughness and its impact on the optical properties in the NIR → UV region [129,130], their implementation is accompanied, however, with many difficulties and challenges (viz., probe fabrication, choosing optimal probe parameters, probing–surface distance, sensitivity of measurements to external parameters, high cost, etc.). Spectroscopic ellipsometry data in the NIR → UV region are required in the Rayleigh–Rice theory [129,130]. For qualitative investigation (especially in the absence of experimental data), it is preferred to consider a phenomenological approach for describing the surface properties. Here, we used a modified 'Drude-Lorentz model' for calculating $R(\omega)/T(\omega)$ in the IR region for GeC/Si (001) materials of different epilayer thicknesses d and charge carrier concentrations η. The simulations have provided valuable information for assessing the role of surface roughness on film δ, film–TL interface δ_2, and conducting TL thickness d_2. Earlier analyses of IR reflectance/transmission spectra and the observations of SEM images in 3C-SiC/Si (001) have shown that the interfacial roughness and conducting layer are related to the carbonization process [96,109].

Our predicted results of $R(\omega)/T(\omega)$ in GeC/Si (001) epilayers have revealed new features at low frequency ($\omega < 626$ cm^{-1} (ω_{TO})) while showing steady downward shifts and a reduction in fringe contrasts at higher frequencies ($\omega > 1600$ cm^{-1}). In undoped epilayers, the angle- and polarization-dependent simulations of reflectance [transmission] have established the Berreman effect [121], revealing (i) a sharp peak [dip] near ω_{TO} in both the s- and p-polarization and (ii) a second dip in p-polarization near the ω_{LO} frequency. In n-doped epilayers, the calculated $R(\omega)$ $[T(\omega)]$ spectrum at oblique incidence has confirmed a peak [dip] near ω_{TO} in p-polarization and an additional dip indicating an η dependent mode at a higher frequency. The high-frequency p-polarized mode shifts to higher values with the increase in η. As this mode, irrespective of η, did not appear in

s-polarization, we therefore assigned it to ω^{+}_{LPP}, given its dependence on η and appearance only in the p-polarization. Based on this study, the Berreman effect in undoped and doped GeC/Si (001) epifilms has provided complementary information to Raman scattering spectroscopy, allowing the identification of ω_{LO}, ω_{TO} phonons and LO-plasmon coupled ω^{+}_{LPP} modes, respectively. In the absence of experimental measurements, our systematic projections of the $(R(\omega)$ and/or $T(\omega))$ spectral profiles have corroborated the results with the existing experimental studies on 3C-SiC/Si (001) epilayers [106–110]. We hope that this work on ultrathin films has the potential to offer a route in exploring the phonon characteristics for different novel GeC-based LDHs, as they are expected to impact many of their optical, electronic, and thermodynamical properties and help in designing different device structures for various technological applications. We strongly feel that the angle- and polarization-dependent predictions of $R(\omega)$ and/or $T(\omega)$ profiles (Berreman effect [121]) in GeC/Si (001) might offer opportunities for spectroscopists to perform similar measurements to check our theoretical conjectures. Systematic calculations of the wave-vector-dependent spectral line shapes for LPP modes in n-doped XC/Si (001) epilayers are necessary for extracting accurate values of the charge carrier concentration η.

Author Contributions: D.N.T. is responsible for the conceptualization, developing methodology, investigations, and computational analysis of the results reported here. J.T.H. checked, reviewed, and edited the original draft. All authors have read and agreed to the published version of the manuscript.

Funding: Institute for Materials Science at Los Alamos National Laboratory, Subcontract #: 616898 (J.T.H).

Data Availability Statement: The data that support the findings of this study are available from the corresponding author upon reasonable request.

Acknowledgments: This work was performed at the Physics Department, University of North Florida in Jacksonville, FL 32224. The author D.T. would like to thank Deanne Snavely, Dean College of Natural Science and Mathematics at Indiana University of Pennsylvania, for the travel support and Innovation Grant that he received from the School of Graduate Studies which made this research possible. J.T.H. acknowledges support from the Institute of Material Science at Los Alamos National Laboratory.

Conflicts of Interest: The authors declare having no financial and/or competing interests.

References

1. Winkler, C. Mittheilungen über das Germanium. *J. Prakt. Chem.* **1887**, *36*, 177. [CrossRef]
2. Winkler, H.C.A.; Lissner, A.; Lange, A.; Prokop, R.; Winkler, R. *Clemens a Detailed Biography*; Akademie Verlag: Berlin, Germany, 1954.
3. Bardeen, J.; Brattain, W.H. The transistor, a semi-conductor triode. *Phys. Rev.* **1948**, *74*, 230. [CrossRef]
4. Shockley, W. The theory of *p-n* junctions in semiconductors and *p-n* junction transistors. *Bell Syst. Tech. J.* **1949**, *28*, 435. [CrossRef]
5. Bell Telephone Laboratories, Inc.; Western Electric Co., Inc. *The Transistor: Selected Reference Material on Characteristics and Applications*; Bell Telephone Laboratories, Inc.: New York, NY, USA, 1951.
6. Wikipedia. History of the Transistor. 23 December 1947. Available online: https://en.wikipedia.org/wiki/History_of_the_transistor (accessed on 26 August 2024).
7. Germanium for Electronic Devices. WK/The New York Times, 10 May 1953. Available online: https://www.nytimes.com/1953/05/10/archives/germanium-forelectronic-devices.html (accessed on 26 August 2024).
8. Lark-Horovitz, K.; Brackett, F.S. The Present State of Physics. In Proceedings of the AAAS Symposium, New York, NY, USA, 30 December 1949; AAAS: Washington, DC, USA, 1950; p. 57.
9. Teal, G.K.; Sparks, M.; Buehler, E. Single crystal germanium. *Proc. IRE* **1952**, *40*, 906–909. [CrossRef]
10. Kilby, J. Miniaturized Electronic Circuits. US Patent 3,138:743, 23 June 1964.
11. Noyce, R. Semiconductor Device-and-Lead Structure. US Patent 2, 981:877, 25 April 1961.
12. Kahng, D.; Atalla, M.M. Silicon-silicon dioxide field induced surface devices. In Proceedings of the IRE-AIEEE Solid-State Device Research Conference, Pittsburgh, PA, USA, 1960.
13. Smith, R.A. *Semiconductors*, 2nd ed.; Cambridge University Press: London, UK, 1979.
14. Emsley, J. *Nature's Building Blocks*, 1st ed.; Oxford University Press: Oxford, UK, 2001.
15. Haller, E. Ge-based devices from materials to devices. *Mater. Sci. Semicond. Process.* **2006**, *9*, 408. [CrossRef]
16. International Technology Roadmap for Semiconductors. Available online: http://www.itrs.net/reports.html (accessed on 26 August 2024).

17. Tiwari, S. *Compound Semiconductor Device Physics*; Academic Press: New York, NY, USA, 1991.
18. Edgar, J.H.; Strite, S.; Akasaki, I.; Amano, H.; Wetzel, C. (Eds.) *Properties, Processing and Applications of Gallium Nitride and Related Semiconductors*; INSPEC: Manchester, UK, 1999.
19. Nakamura, S.; Chichibu, S.F. (Eds.) *Introduction to Nitride Semiconductor Blue Lasers and Light Emitting Diodes*; Taylor & Francis: Abingdon-on-Thames, UK, 2000.
20. Schubert, E.F. *Light-Emitting Diodes*; Cambridge University Press: London, UK, 2003.
21. Zhou, S.; Liao, Z.; Sun, K.; Zhang, Z.; Qian, Y.; Liu, P.; Du, P.; Jiang, J.; Lv, Z.; Qi, S. High-Power AlGaN-Based Ultrathin Tunneling Junction Deep Ultraviolet Light-Emitting Diodes. *Laser Photonics Rev.* **2024**, *18*, 2300464. [CrossRef]
22. Liu, Z.; Nong, M.; Lu, Y.; Cao, H.; Yuvaraja, S.; Xiao, N.; Alnakhli, Z.; Vázquez, R.; Li, X. Effect of the AlN strain compensation layer on InGaN quantum well red-light-emitting diodes beyond epitaxy. *Opt. Lett.* **2022**, *47*, 6230. [CrossRef] [PubMed]
23. Rickman, A. The commercialization of silicon photonics. *Nat. Photonics* **2014**, *8*, 579–582. [CrossRef]
24. Komljenovic, T.; Davenport, M.; Hulme, J.; Liu, A.Y.; Santis, C.T.; Spott, A.; Srinivasan, S.; Stanton, E.J.; Zhang, C.; Bowers, J.E. Heterogeneous Silicon Photonic Integrated Circuits. *J. Light. Technol.* **2016**, *34*, 20–35. [CrossRef]
25. Dong, P.; Liu, X.; Chandrasekhar, S.; Buhl, L.L.; Aroca, R.; Chen, Y.K. Monolithic Silicon Photonic Integrated Circuits for Compact 100+Gb/s Coherent Optical Receivers and Transmitters. *IEEE J. Sel. Top. Quantum Electron.* **2014**, *20*, 150–157. [CrossRef]
26. Horikawa, T.; Shimura, D.; Okayama, H.; Jeong, S.-H.; Takahashi, H.; Ushida, J.; Sobu, Y.; Shiina, A.; Tokushima, M.; Kinoshita, K.; et al. A 300-mm Silicon Photonics Platform f, or Large-Scale Device Integration. *IEEE J. Sel. Top. Quantum Electron.* **2018**, *24*, 8200415. [CrossRef]
27. Kukushkin, S.; Osipov, A.; Redkov, A. SiC/Si as a New Platform for Growth of Wide-Bandgap Semiconductors. In *Mechanics and Control of Solids and Structures, Advanced Structured Materials*; Polyanskiy, V.A., Belyaev, A.K., Eds.; Springer Nature Switzerland AG: Cham, Switzerland, 2022; Volume 164, Chapter 18; pp. 335–367; ISBN 978-3-030-93076-9; (eBook). [CrossRef]
28. Nguyen, T.-K.; Yadav, S.; Truong, T.-A.; Han, M.; Barton, M.; Leitch, M.; Guzman, P.; Dinh, T.; Ashok, A.; Vu, H.; et al. Integrated, Transparent Silicon Carbide Electronics and Sensors for Radio Frequency Biomedical Therapy. *ACS Nano* **2022**, *16*, 10890–10903. [CrossRef] [PubMed]
29. Pham, T.A.; Nguyen, T.K.; Vadivelu, R.K.; Dinh, T.; Qamar, A.; Yadav, S.; Yamauchi, Y.; Rogers, J.A.; Nguyen, N.T.; Phan, H.P. Stretchable Bioelectronics: A Versatile Sacrificial Layer for Transfer Printing of Wide Bandgap Materials for Implantable and Stretchable Bioelectronics. *Adv. Funct. Mater.* **2020**, *30*, 2070287. [CrossRef]
30. Nguyen, T.K.; Phan, H.P.; Kamble, H.; Vadivelu, R.; Dinh, T.; Iacopi, A.; Walker, G.; Hold, L.; Nguyen, N.T.; Dao, D.V. Superior Robust Ultrathin Single-Crystalline Silicon Carbide Membrane as a Versatile Platform for Biological Applications. *ACS Appl. Mater. Interfaces* **2017**, *9*, 41641–41647. [CrossRef]
31. Kazanskiy, N.L.; Khonina, S.N.; Butt, M.A. Advancement in Silicon Integrated Photonics Technologies for Sensing Applications in Near-Infrared and Mid-Infrared Region: A Review. *Photonics* **2022**, *9*, 331. [CrossRef]
32. Selim, R.; Hoofman, R.; Khoder, M.; Masood, A.; Littlejohns, C.; Geuzebroek, D.; Grootjans, R.; Drischel, T.; Torki, K. Silicon photonics open access foundry services review for emerging technology. In Proceedings of the SPIE, Glasgow, Scotland, UK, 28 September–1 October 2021; Emerging Applications in Silicon Photonics II, 118800C; Volume 11880. [CrossRef]
33. Dan, L.; Citrin, D.S.; Hu, S. Compact high-performance polarization beam splitter based on a silicon photonic crystal heterojunction. *Opt. Mater.* **2020**, *109*, 110256.
34. Maram, R.; Kaushal, S.; Azaña, J.; Chen, L.R. Recent Trends and Advances of Silicon-Based Integrated Microwave Photonics. *Photonics* **2019**, *6*, 13. [CrossRef]
35. Chen, G.R.; Choi, J.W.; Sahin, E.; Ng, D.T.; Tan, D.H. On-chip 1 by 8 coarse wavelength division multiplexer and multi-wavelength source on ultra-silicon-rich nitride. *Opt. Express* **2019**, *27*, 23549–23557. [CrossRef]
36. Rahim, A.; Spuesens, T.; Baets, R.; Bogaerts, W. Open-Access Silicon Photonics: Current Status and Emerging Initiatives. *Proc. IEEE* **2018**, *106*, 2313–2330. [CrossRef]
37. Dai, D.X.; Wang, S.P. Asymmetric directional couplers based on silicon nanophotonic waveguides and applications. *Front. Optoelectron.* **2016**, *9*, 450–465. [CrossRef]
38. EUROPRACITCE-IC. Available online: http://www.europractice-ic.com (accessed on 26 August 2024).
39. CORNERSTONE. Available online: https://www.cornerstone.sotonfab.co.uk (accessed on 26 August 2024).
40. Littlejohns, C.G.; Rowe, D.J.; Du, H.; Li, K.; Zhang, W.; Cao, W.; Dominguez Bucio, T.; Yan, X.; Banakar, M.; Tran, D.; et al. CORNERSTONE's Silicon Photonics Rapid Prototyping Platforms: Current Status and Future Outlook. *Appl. Sci.* **2020**, *10*, 8201. [CrossRef]
41. GlobalFoundries. Available online: http://www.globalfoundries.com/ (accessed on 26 August 2024).
42. Silicon Photonic IC Prototyping. Available online: https://www.imeciclink.com/en/asic-fabrication/si (accessed on 26 August 2024).
43. Bennett, H.S.; Brederlow, R.; Costa, J.C.; Cottrell, P.E.; Huang, W.M.; Immorlica, A.A., Jr.; Mueller, J.-E.; Racanelli, M.; Shichijo, H.; Weitzel, C.E.; et al. Device and Technology Evolution for Si-Based RF Integrated Circuits. *IEEE Trans. Electron Dev.* **2005**, *52*, 1235. [CrossRef]
44. Gutmann, R.J. Advanced Silicon IC Interconnect Technology and Design: Present Trends and RF Wireless Implications. *IEEE Trans. Microw. Theory Tech.* **1999**, *47*, 667. [CrossRef]

45. Burghartz, J.N. Silicon RF technology—The two generic approaches. In Proceedings of the 27th European Solid-State Device Research Conference, Stuttgart, Germany, 22–24 September 1997; pp. 143–153.
46. Razavi, B. CMOS technology characterization for analog and RF design. *IEEE J. Sol. St. Circ.* **1999**, *34*, 268–276. [CrossRef]
47. Liang, X.; Wang, H.; Wang, C. Lattice thermal conductivity of transition metal carbides: Evidence of a strong electron-phonon interaction above room temperature. *Acta Mater.* **2021**, *216*, 117160. [CrossRef]
48. Saleem, A.; Zhang, Y.; Gong, H.; Majeed, M.K. Fluoride doped SiC/Si_3N_4 composite as a high thermal conductive material with enhanced mechanical properties. *Ceram. Int.* **2019**, *45*, 21004–21010. [CrossRef]
49. Yang, H.; Ma, Y.; Da, Y. Progress of structural and electronic properties of diamond: A mini review. *Funct. Diam.* **2021**, *1*, 150–159. [CrossRef]
50. Yue, Y.; Gao, Y.; Hu, W.; Xu, B.; Wang, J.; Zhang, X.; Zhang, Q.; Wang, Y.; Ge, B.; Yang, Z.; et al. Hierarchically structured diamond composite with exceptional Toughness. *Nature* **2020**, *582*, 370. [CrossRef]
51. Huang, Q.; Yu, D.; Xu, B.; Hu, W.; Ma, Y.; Wang, Y.; Zhao, Z.; Wen, B.; He, J.; Liu, Z.; et al. Nano twinned diamond with unprecedented hardness and stability. *Nature* **2014**, *510*, 250–253. [CrossRef]
52. Bauer, M.R.; Tolle, J.; Bungay, C.; Chizmeshya, A.V.G.; Smith, D.J.; Menéndez, J.; Kouvetakis, J. Tunable band structure in diamond–cubic tin–germanium alloys grown on silicon substrates. *Solid State Commun.* **2003**, *127*, 355–359. [CrossRef]
53. Islam, M.S.; Mojumder, R.H.; Hassan, A.; Sohag, M.U.; Park, J. High-Efficiency Multi Quantum Well Blue LED Using 2D-SiC as an Active Material. In Proceedings of the 5th International Conference on Electrical Engineering and Information & Communication Technology (ICEEICT) Military Institute of Science and Technology (MIST), Dhaka, Bangladesh, 18–20 November 2021. [CrossRef]
54. Ikoma, Y.; Endo, T.; Watanabe, F.; Motooka, T. Growth of Ultrathin Epitaxial 3C-SiC Films on Si(100) by Pulsed Supersonic Free Jets of CH_3SiH_3. *Jpn. J. Appl. Phys.* **1999**, *38*, L301. [CrossRef]
55. Ohtani, R.; Ikoma, Y.; Motooka, T. Formation of Si/SiC heterostructures for silicon-based quantum devices using single CH_3SiH_3-gas source free jet. *Mat. Res. Soc. Symp. Proc.* **2004**, *815*, 118–123. [CrossRef]
56. Ikoma, Y.; Endo, T.; Watanabe, F.; Motooka, T. Growth of Si/3C–SiC/Si(100) heterostructures by pulsed supersonic free jets. *Appl. Phys. Lett.* **1999**, *75*, 3977. [CrossRef]
57. Okinaka, M.; Hamana, Y.; Tokuda, T.; Ohta, J.; Nunoshita, M. MBE growth mode and C incorporation of GeC epilayers on Si(0 0 1) substrates using an arc plasma gun as a novel C source. *J. Cryst. Growth* **2003**, *249*, 78–86. [CrossRef]
58. Dey, T.; Reza, M.S.; Arbogast, A.W.; Holtz, M.; Droopad, R.; Bank, S.R.; Wistey, M.A. Molecular beam epitaxy of highly crystalline GeSnC using CBr4 at low temperatures. *Appl. Phys. Lett.* **2022**, *121*, 122104. [CrossRef]
59. Dey, T.; Arbogast, A.W.; Meng, Q.; Reza, M.S.; Muhowski, A.J.; Cooper, J.P.; Ozdemir, E.; Naab, F.U.; Borrely, T.; Anderson, J.; et al. Influence of H on Sn incorporation in GeSnC alloys grown using molecular beam epitaxy. *J. Appl. Phys.* **2023**, *134*, 193102. [CrossRef]
60. Talwar Devki, N.; Feng, Z.C.; Liu, C.W.; Tin, C.-C. Influence of surface roughness and interfacial layer on the infrared spectra of V-CVD grown 3C-SiC/Si (1 0 0) epilayers. *Semicond. Sci. Technol.* **2012**, *27*, 115019. [CrossRef]
61. Yoshimura, S.; Sugimoto, S.; Takeuchi, T.; Murai, K.; Kiuchi, M. Low energy Si+, SiCH5+, or C+ beam injections to silicon substrates during chemical vapor deposition with dimethyl silane. *Heliyon* **2023**, *9*, e19002. [CrossRef]
62. Li, X.; Jacobson, H.; Boulle, A.; Chaussende, D.; Henry, A. Double-Position-Boundaries Free 3C-SiC Epitaxial Layers Grown on On-Axis 4H-SiC. *ECS J. Solid State Sci. Technol.* **2014**, *3*, 75. [CrossRef]
63. Xin, B.; Jia, R.X.; Hu, J.C.; Tsai, C.Y.; Lin, H.H.; Zhang, Y.M. A step-by-step experiment of 3C-SiC hetero-epitaxial growth on 4H-SiC by CVD. *Appl. Surf. Sci.* **2015**, *357*, 985–993. [CrossRef]
64. Wu, J.; Qian, S.T.; Huo, T.G.; Zheng, J.X.; Zhang, P.L.; Dai, Y.; Geng, D.S. Effect of PyC Inner Coating on Preparation of 3C-SiC Coating on Quartz Glass by Chemical Vapor Reaction. *Front. Mater.* **2022**, *9*, 897900. [CrossRef]
65. Kaloyeros, A.E.; Arkles, B. Silicon Carbide Thin Film Technologies: Recent Advances in Processing, Properties, and Applications—Part I Thermal and Plasma CVD. *ECS J. Solid State Sci. Technol.* **2023**, *12*, 103001. [CrossRef]
66. Huguenin-Love, J.; Soukup, R.; Ianno, N.; Schrader, J.; Thompson, D.; Dalal, V. Optical and crystallographic analysis of thin films of GeC deposited using a unique hollow cathode sputtering technique. *Mater. Sci. Semicond.* **2006**, *9*, 759. [CrossRef]
67. Hartmanna, J.M.; Abbadiea, A.; Vineta, M.; Claveliera, L.; Holligera, P.; Lafonda, D.; Semeria, M.N.; Gentile, P. Growth kinetics of Si on fullsheet, patterned and silicon-on-insulator substrates. *J. Cryst. Growth* **2003**, *257*, 19–30. [CrossRef]
68. Kawanishi, S.; Daikoku, H.; Shibata, H.; Yoshikawa, T. Suppressing solvent compositional change during solution growth of SiC using SiC/C gradient crucible. *J. Cryst. Growth* **2021**, *576*, 126382. [CrossRef]
69. Sannodo, N.; Osumi, A.; Kaminaga, K.; Maruyama, S.; Matsumoto, Y. Vapor-liquid-solid-like growth of high-quality and uniform 3C-SiC heteroepitaxial films on alpha-Al_2O_3 (0001) substrates. *Cryst. Eng. Comm.* **2021**, *23*, 1709–1717. [CrossRef]
70. Kukushkin, S.A.; Osipov, A.V. Epitaxial silicon carbide on silicon. method of coordinated substitution of atoms (a review). *Russ. J. Gen. Chem.* **2022**, *92*, 584. [CrossRef]
71. Gupta, N.; Veetil, B.P.; Xia, H.; Karuturi, S.K.; Conibeer, G.; Shrestha, S. Synthesis of nano-crystalline germanium carbide using radio frequency magnetron sputtering. *Thin Solid Films* **2015**, *592*, 162. [CrossRef]
72. Booth, D.C.; Voss, K.J. The optical and structural properties of CVD germanium carbide. *J. Phys. Colloq.* **1981**, *42*, C4–C1033. [CrossRef]
73. Feldman, D.W.; Parker, J.H., Jr.; Choyke, W.J.; Patrick, L. Phonon Dispersion Curves by Raman Scattering in SiC, Polytypes 3C, 4H, 6H, 15R, and 21R. *Phys. Rev.* **1968**, *173*, 787. [CrossRef]

74. Yoshida, M.; Onodera, A.; Ueno, M.; Takemura, K.; Shimomura, O. Pressure-induced phase transition in SiC. *Phys. Rev. B* **1993**, *48*, 10587. [CrossRef]
75. Olego, D.; Cardona, M.; Vogl, P. Pressure dependence of the optical phonons and transverse effective charge in 3C-SiC. *Phys. Rev. B* **1982**, *25*, 3878. [CrossRef]
76. Serrano, J.; Strempfer, J.; Cardona, M.; Schwoerer-Böhning, M.; Requardt, H.; Lorenzen, M.; Stojetz, B.; Pavone, P.; Choyke, W.J. Determination of the phonon dispersion of zinc blende (3C) silicon carbide by inelastic x-ray scattering. *Appl. Phys. Lett.* **2002**, *80*, 4360. [CrossRef]
77. Adachi, S. *Properties of Semiconductor Alloys: Group-IV, III-V and II-VI, Semiconductors*; Wiley: Hoboken, NJ, USA, 2009.
78. Available online: https://www.ioffe.ru/SVA/NSM/Semicond/Si/optic.html (accessed on 26 August 2024).
79. Majid, A. A perspective on non-stoichiometry in silicon carbide (review article). *Ceram. Int.* **2018**, *44*, 1277. [CrossRef]
80. Hao, A.; Yang, X.C.; Wang, X.M.; Zhu, Y.; Liu, X.; Liu, R.P. First-principles investigations on electronic, elastic, and optical properties of XC (X = Si, Ge, and Sn) under high pressure. *J. Appl. Phys.* **2010**, *108*, 063531. [CrossRef]
81. Jankousky, M.; Garrity, E.M.; Stevanovic, V. Polymorphism of group-IV carbides: Structures, (meta)stability, electronic, and transport properties. *Phys. Rev. Mat.* **2023**, *7*, 053606. [CrossRef]
82. Wang, C.Z.; Yu, R.C.; Krakauer, H. Pressure dependence of Born effective charges, dielectric constant, and lattice dynamics in SiC. *Phys. Rev. B* **1996**, *53*, 5430. [CrossRef]
83. Souadkia, M.; Bennecer, B.; Kalarasse, F. Elastic, vibrational and thermodynamic properties of α-Sn based group IV semiconductors and GeC under pressure. *J. Phys. Chem. Solids* **2013**, *74*, 1615–1625. [CrossRef]
84. Zhang, X.; Quan, S.; Ying, C.; Li, Z. Theoretical investigations on the structural, lattice dynamical and thermodynamic properties of XC (X = Si, Ge, Sn). *Solid State Commun.* **2011**, *151*, 1545–1549. [CrossRef]
85. Pandey, R.; Rérat, M.; Darrigan, C.; Causà, M. A theoretical study of stability, electronic, and optical properties of GeC and SnC. *J. Appl. Phys.* **2000**, *88*, 6462. [CrossRef]
86. Davydov, S.Y.; Lebedev, A. Dielectric and optical properties of the cubic SiC, GeC and SnC monocrystals: Model estimations. *Phys. Solid State* **2022**, *64*, 68. [CrossRef]
87. Sahnoun, M.; Khenata, R.; Baltache, H.; Rérat, M.; Driz, M.; Bouhafs, B.; Abbar, B. First-principles calculations of optical properties of GeC, SnC and GeSn under hydrostatic pressure. *Physica B* **2005**, *355*, 392. [CrossRef]
88. Sekkal, W.; Zaoui, A. Predictive study of thermodynamic properties of GeC. *New J. Phys.* **2022**, *4*, 9. [CrossRef]
89. Abdulsattar, M.A.; Almaroof, S.M. Electronic and spectroscopic properties of GeC superlattice nanocrystals: A first-principles study using diamondoid structures. *Superlattices Microstruct.* **2015**, *79*, 63–71. [CrossRef]
90. Saito, N.; Yamaguchi, T.; Nakaaki, I. Comparative study of properties between *a*-GeC:H and *a*-SiC:H films prepared by radio-frequency reactive sputtering in methane. *J. Appl. Phys.* **1995**, *78*, 3949–3954. [CrossRef]
91. Bayu Aji, L.B.; Stavrou, E.; Wallace, J.B.; Boulle, A.; Debelle, A.; Kucheyev, S.O. Comparative study of radiation defect dynamics in 3C-SiC by X-ray diffraction, Raman scattering, and ion channeling. *Appl. Phys. A* **2019**, *125*, 1. [CrossRef]
92. Boulle, A.; Debelle, A.; Wallace, J.B.; Aji, L.B.; Kucheyev, S.O. The amorphization of 3C-SiC irradiated at moderately elevated temperatures as revealed by X-ray diffraction. *Acta Mater.* **2017**, *140*, 250. [CrossRef]
93. Zhang, L.; Jiang, W.; Pan, C.; Fadanelli, R.C.; Ai, W.; Chen, L.; Wang, T. Raman study of amorphization in nanocrystalline 3C–SiC irradiated with C.+ and He+ ions. *J. Raman Spectrosc.* **2019**, *50*, 1197. [CrossRef]
94. Lindner, J.K.N.; Tsang, W.M.; Wong, S.P.; Xu, J.B.; Wilson, I.H. XTEM characterization of tungsten implanted SiC thin films on silicon for field emission devices. *Thin Solid Films* **2003**, *427*, 417–421. [CrossRef]
95. Scuderi, V.; Calabretta, C.; Anzalone, R.; Mauceri, M.; La Via, F. Characterization of 4H- and 6H-Like Stacking Faults in Cross Section of 3C-SiC Epitaxial Layer by Room-Temperature μ-Photoluminescence and μ-Raman Analysis. *Materials* **2020**, *13*, 1837. [CrossRef]
96. Talwar Devki, N. Spectroscopic Investigations for the Dynamical Properties of Defects in Bulk and Epitaxially Grown 3C-SiC/Si (100). In *Handbook of Silicon Carbide Materials and Devices*; Feng, Z.C., Ed.; CRC: Boca Raton, FL, USA, 2023; Chapter 3.
97. Varshney, D.; Shriya, S.; Varshney, M.; Singh, N.; Khenata, R. Elastic and thermo-dynamical properties of cubic (3C) silicon carbide under high pressure and high temperature. *J. Theor. Appl. Phys.* **2015**, *9*, 221–249. [CrossRef]
98. Sfuncia, G.; Nicotra, G.; Giannazzo, F.; Pécz, B.; Gueorguiev, G.K.; Kakanakova-Georgieva, A. 2D graphitic-like gallium nitride and other structural selectivity in confinement at the graphene/SiC interface. *Cryst. Eng. Comm.* **2023**, *25*, 5810–5817. [CrossRef]
99. Pela, R.R.; Hsiao, C.-L.; Hultman, L.; Birch, J.; Gueorguiev, G.K. Electronic and optical properties of core–shell InAlN nanorods: A comparative study via LDA, LDA-1/2, mBJ, HSE06, G_0W_0 and BSE methods. *Phys. Chem.* **2024**, *26*, 7504–7514. [CrossRef] [PubMed]
100. Gallagher, J.D.; Senaratne, C.L.; Kouvetakis, J.; Menéndez, J. Compositional dependence of the bowing parameter for the direct and indirect band gaps in Ge1-ySny alloys. *Appl. Phys. Lett.* **2014**, *105*, 142102.
101. Ghetmiri, S.A.; Du, W.; Margetis, J.; Mosleh, A.; Cousar, L.; Conley, B.R.; Domulevicz, L.; Nazzal, A.; Sun, G.; Soref, R.A.; et al. Direct-bandgap GeSn grown on silicon with 2230 nm photoluminescence. *Appl. Phys. Lett.* **2014**, *105*, 6. [CrossRef]
102. Wirths, S.; Geiger, R.; von den Driesch, N.; Mussler, G.; Stoica, T.; Mantl, S.; Ikonic, Z.; Luysberg, M.; Chiussi, S.; Hartmann, J.M.; et al. Lasing in direct-bandgap GeSn alloy grown on Si. *Nat. Photonics* **2015**, *9*, 88. [CrossRef]
103. Xu, Z.; Li, Y.Z.; Liu, Z. Controlling electronic and optical properties of layered SiC and GeC sheets by strain engineering. *Mater. Des.* **2016**, *108*, 333–342. [CrossRef]

104. Xua, Q.; Cai, W.; Li, W.; Sreeprasad, T.S.; He, Z.; Ong, W.-J.; Li, N. Two-dimensional quantum dots: Fundamentals, photoluminescence mechanism and their energy and environmental applications. *Mater. Today Energy* **2018**, *10*, 222–240. [CrossRef]
105. Schulte-Braucks, C.; Glass, S.; Hofmann, E.; Stange, D.; von den Driesch, N.; Hartmann, J.M.; Ikonic, Z.; Zhao, Q.T.; Buca, D.; Mantl, S. Process modules for GeSn nanoelectronics with high Sn-contents. *Solid State Electron.* **2017**, *128*, 54–59. [CrossRef]
106. Holm, R.T.; Klein, P.H.; Nordquist, P.E.R. Infrared reflectance evaluation of chemically vapor deposited b-SiC films grown on Si substrates. *J. Appl. Phys.* **1986**, *60*, 1479. [CrossRef]
107. Engelbrecht, J.A.A.; van Rooyen, I.J.; Henry, A.; Janzén, E.; Olivier, E.J. The origin of a peak in the reststrahlen region of SiC. *Physica B* **2012**, *407*, 1525–1528. [CrossRef]
108. MacMillan, M.F.; Devaty, R.P.; Choyke, W.J.; Goldstein, D.R.; Spanier, J.E.; Kurtz, A.D. Infrared reflectance of thick p-type porous SiC layers. *J. Appl. Phys.* **1996**, *80*, 2412–2419. [CrossRef]
109. Dong, L.; Sun, G.; Zheng, L.; Liu, X.; Zhang, F.; Yan, G.; Zhao, W.; Wang, L.; Li, X.; Wang, Z. Infrared reflectance study of 3C-SiC epilayers grown on silicon substrates. *J. Phys. D Appl. Phys.* **2012**, *45*, 245102. [CrossRef]
110. Pascual, J.; Ben el Mekki, M.; Arnaud, G.; Camassel, J. *Roughness Effects in the Infrared Reflectance of Thick 3C-SiC Films on Si Substrates*; SPIE: Bellingham, WA, USA, 1995; Volume 2648, p. 12.
111. Heavens, O.S. *Optical Properties of Thin Solid Films*; Butterworths Scientific Publications: London, UK, 1955.
112. Piro, O.E. Optical properties, reflectance, and transmittance of anisotropic absorbing crystal plates. *Phys. Rev. B* **1987**, *36*, 3427. [CrossRef] [PubMed]
113. Talwar, D.N.; Feng, Z.C. Understanding spectroscopic phonon-assisted defect features in CVD grown 3C-SiC/Si (100) by modeling and simulation. *Comput. Mater. Sci.* **2004**, *30*, 419. [CrossRef]
114. Cadman, T.W.; Sadowski, D. Generalized equations for the calculation of absorptance, reflectance, and transmittance of a number of parallel surfaces. *Appl. Opt.* **1978**, *17*, 531. [CrossRef]
115. Talwar, D.N.; Yang, T.R.; Feng, Z.C.; Becla, P. Infrared reflectance and transmission spectra in II-VI alloys and superlattices. *Phys. Rev. B* **2011**, *84*, 174203. [CrossRef]
116. Shokhovets, S.; Goldhahn, R.; Cimalla, V.; Cheng, T.S.; Foxon, C.T. Reflectivity study of hexagonal GaN films grown on GaAs: Surface roughness, interface layer, and refractive index. *J. Appl. Phys.* **1998**, *84*, 1561. [CrossRef]
117. Landron, O.; Feuerstein, M.J.; Rappaport, T.S. In Situ Microwave Reflection Coefficient Measurements for Smooth and Rough Exterior Wall Surfaces. In Proceedings of the IEEE Vehicular Technology Conference, Secaucus, NJ, USA, 18–20 May 1993; p. 77.
118. Talwar Devki, N. Composition dependent phonon and thermodynamical characteristics of C-based $X_xY_{1-x}C$ (X, Y≡ Si, Ge, Sn) alloys. *Inorg. Inorg.* **2024**, *12*, 100. [CrossRef]
119. Inamoto, S.; Yamasaki, J.; Tamaki, H.; Tanaka, N. Atomic arrangement at the 3C-SiC/Si(001) interface revealed utilizing aberration-corrected transmission electron microscope. *Philos. Mag. Lett.* **2011**, *91*, 632. [CrossRef]
120. Orlov, L.K.; Drozdov, Y.N.; Drozdov, M.N.; Pod'yacheva, O.A.; Vdovin, V.I. A comprehensive structural analysis of silicon carbide layers grown by vacuum epitaxy on silicon from hydrides and hydrocarbons. *J. Struct. Chem.* **2010**, *51*, S145. [CrossRef]
121. Berreman, D.W. Resonant Reflectance Anomalies: Effect of Shapes of Surface Irregularities. *Phys. Rev. B* **1970**, *1*, 381. [CrossRef]
122. Geurts, J. Raman spectroscopy from buried semiconductor interfaces: Structural and electronic properties. *Phys. Status Solidi B* **2015**, *252*, 19–29. [CrossRef]
123. Ochoa, M.A.; Maslar, J.E.; Bennett, H.S. Extracting electron densities in n-type GaAs from Raman spectra: Comparisons with Hall measurements. *J. Appl. Phys.* **2020**, *128*, 075703. [CrossRef] [PubMed]
124. Mao, Z.; Fu, C.; Pan, X.; Chen, X.; He, H.; Wang, W.; Zeng, Y.; Ye, Z. Raman-based measurement of carrier concentration in n-type ZnO thin films under resonant conditions. *Phys. Lett. A* **2020**, *384*, 126148. [CrossRef]
125. Abstreiter, G.; Cardona, M.; Pinczuk, A. Light Scattering by Free Carrier Excitations in Semiconductors. In *Light Scattering in Solids IV, Topics in Applied Physics*; Springer: Berlin/Heidelberg, Germany, 1984; pp. 5–150.
126. Kukharskii, A.A. Plasmon-phonon coupling in GaAs. *Sol. State Commun.* **1973**, *13*, 1371. [CrossRef]
127. Caughey, D.M.; Thomas, R.E. Carrier Mobilities in Silicon Empirically Related to Doping and Field. *Proc. IEEE* **1967**, *55*, 2192–2193. [CrossRef]
128. Paetzelt, H.; Böhm, G.; Arnold, T. Etching of silicon surfaces using atmospheric plasma jets. *Plasma Sources Sci. Technol.* **2015**, *24*, 025002. [CrossRef]
129. Franta, D.; Ohlídal, I. Influence of lateral dimensions of the irregularities on the optical quantities of rough surfaces. *J. Opt. A Pure Appl. Opt.* **2006**, *8*, 763. [CrossRef]
130. Ohlídal, I.; Vohánka, J.; Čermák, M.; Franta, D. Combination of spectroscopic ellipsometry and spectroscopic reflectometry with including light scattering in the optical characterization of randomly rough silicon surfaces covered by native oxide layers. *Surf. Topogr. Metrol. Prop.* **2019**, *7*, 045004. [CrossRef]